

A quantum defect model for the *s*, *p*, *d*, and *f* Rydberg series of CaF

Jeffrey J. Kay,¹ Stephen L. Coy,¹ Bryan M. Wong,¹ Christian Jungen,^{2,3} and Robert W. Field^{1,a)}

¹Department of Chemistry, Massachusetts Institute of Technology, Cambridge, Massachusetts 02139, USA

²Laboratoire Aimé Cotton du CNRS, Université de Paris Sud, Bâtiment 505, F-91405 Orsay, France

³Department of Physics and Astronomy, University College London, London WC1E 6BT, United Kingdom

(Received 20 September 2010; accepted 18 February 2011; published online 18 March 2011)

We present an improved quantum defect theory model for the “*s*,” “*p*,” “*d*,” and “*f*” Rydberg series of CaF. The model, which is the result of an exhaustive fit of high-resolution spectroscopic data, parameterizes the electronic structure of the ten (“*s*” Σ , “*p*” Σ , “*p*” Π , “*d*” Σ , “*d*” Π , “*d*” Δ , “*f*” Σ , “*f*” Π , “*f*” Δ , and “*f*” Φ) Rydberg series of CaF in terms of a set of twenty $\mu_{\ell\ell}^{(A)}$ quantum defect matrix elements and their dependence on both internuclear separation and on the binding energy of the outer electron. Over 1000 rovibronic Rydberg levels belonging to 131 observed electronic states of CaF with $n^* \geq 5$ are included in the fit. The correctness and physical validity of the fit model are assured both by our intuition-guided combinatorial fit strategy and by comparison with R-matrix calculations based on a one-electron effective potential. The power of this quantum defect model lies in its ability to account for the rovibronic energy level structure and nearly all dynamical processes, including structure and dynamics outside of the range of the current observations. Its completeness places CaF at a level of spectroscopic characterization similar to NO and H₂. © 2011 American Institute of Physics. [doi:10.1063/1.3565967]

I. INTRODUCTION

Understanding the mechanisms of energy flow within molecules is central to a fundamental understanding of chemical phenomena.¹ However, characterizing the pathways along which energy is transferred is difficult, especially for large and highly excited molecules. The number of pathways that energy follows in the redistribution process grows rapidly with the number of available modes of excitation, and new energy transfer pathways become available as the total internal energy of the molecule increases. Even for diatomic molecules, a complete and *mechanistic* understanding of—or even a complete *phenomenological* numerical model for—energy flow at the quantum state level does not exist.²

Before we can understand *where*, *why*, and *how* energy flows in a molecule, we must first develop a model that is capable of describing *what* actually happens. Energy flow in molecules is usually described in the framework of the Born–Oppenheimer (BO) approximation.³ In the Born–Oppenheimer approximation, the molecular Hamiltonian is divided into electronic and nuclear terms, with molecular wavefunctions expressed as Born–Oppenheimer products of electronic and nuclear wavefunctions. Eigenstate energies obtained by solving the electronic Schrödinger equation are used to construct a set of adiabatic potential energy surfaces, which govern the motion of the nuclei. Solution of the nuclear Schrödinger equation gives the vibrational and rotational energies, and the total energy of the molecule is expressed as

$$E_{\text{tot}} = E_{\text{el}} + E_{\text{vib}} + E_{\text{rot}}, \quad (1)$$

^{a)}Author to whom correspondence should be addressed. Electronic mail: rwfield@mit.edu.

which reflects the partitioning of the Hamiltonian into electronic, vibrational, and rotational parts. The Born–Oppenheimer approximation works well at low energy, where the mismatch in timescales of electronic and nuclear motions prevents interconversion of energy, and the intramolecular dynamics is simple and usually restricted to one potential energy surface. Inevitably, as a molecule acquires more electronic energy, the Born–Oppenheimer approximation fails: potential energy curves become closely spaced and diabatic curves of states belonging to different electronic configurations cross. For very highly excited states, these Born–Oppenheimer-breakdown effects become the rule, rather than its exception.

Molecular Rydberg states typify this type of atypical behavior. As the energy increases along a Rydberg series, the classical frequency of electronic motion becomes progressively slower, eventually becoming so slow that electronic motion occurs on the same time scale as vibration, rotation, and even electron or nuclear spin processes.^{4–8} When electronic motion tunes into resonance with another motion, energy exchange between the Rydberg electron and the molecular ion-core becomes rapid and efficient, resulting in extensively fragmented energy level patterns and a near-complete loss of regularity.⁹ Intersections between Rydberg and (typically multiple) valence potential energy curves result, even in the simplest molecules, in a hopelessly tangled web of interacting states. These effects simply cannot be described within the framework of the Born–Oppenheimer approximation. In fact, for the vast majority of chemically relevant state space, the Born–Oppenheimer picture is the *wrong* picture entirely. Fortunately, an *appropriate* picture does exist.

Often, when one representation fails catastrophically, another representation comes to the rescue. Multichannel quantum defect theory (MQDT) (Refs. 10–20) is *designed* to go beyond the Born–Oppenheimer approximation. It accomplishes this by applying the Born–Oppenheimer approximation *only in the region of coordinate space where it is appropriate*—that is, where all electrons are near the nuclei and moving quickly with respect to vibration and rotation. Scattering theory is then used to ensure that the wavefunction of the system is described properly outside of this region. Quantum defect theory (QDT) can be used to compute all of the energy levels of a molecule, including the non-Born–Oppenheimer interactions among the zero-order states contained in each eigenstate, as well as interactions of the nominally bound Rydberg states with ionization and dissociation continua. The only shortcoming of quantum defect theory is that the key parameters that describe these interactions, the quantum defects, cannot be estimated *a priori* based on physical intuition or analogy to another molecule; the quantum defects must either be calculated (using *ab initio* or semiempirical methods) or determined directly from a fit to experimental data. Quantum defect theory provides the framework, but the model itself must be constructed on a case-by-case basis, individually for each molecule.

Here, we extend our quantum defect model for our prototypical Rydberg molecule, CaF, to include almost all possible dynamical effects sampled by the vast quantity of experimental data presently available. CaF has been studied for decades^{21–31} and the energies of all of its “s,” “p,” “d,” and “f” Rydberg states, from the ground state of the molecule to the vibrationally excited Rydberg states that lie above the $v = 0$ ionization limit, are now known to spectroscopic accuracy (to within $\sim 0.01\text{--}0.10\text{ cm}^{-1}$). CaF is an *unusually simple* molecule: nearly all of its electronic states, including even the electronic ground state, are Rydberg states, due to the closed-shell nature (Ca^{2+}F^-) of the ion-core. Although non-Rydberg covalent ($\text{Ca}^\circ\text{F}^0$) states do exist (and even these can be thought of as lowest members of a Rydberg series built on an electronically excited Ca^+F^0 ion-core), none are strongly bound, due to the lack of strong ionic or covalent interactions between the constituent atoms in the electronically excited Ca^+F^0 core upon which these covalent states are built. The interactions between the Rydberg states and the (repulsive) covalent states are weak and mainly result in predissociation of the Rydberg levels. CaF is thus one of the *simpler possible* molecules, combining the electronic simplicity of an alkali atom with the structural simplicity of a diatomic molecule.

In this work, we subject all Rydberg states with effective principal quantum number $n^* \geq 5.0$ to an extensive fit process in order to determine the diagonal and off-diagonal elements of the molecular quantum defect matrix and the dependences of these elements on the internuclear distance and the collision energy of the outer electron. The input data span a wide range of electronic, vibrational, and rotational quantum numbers, and the states included in the data set participate in a wide range of classes of nonadiabatic interactions. The resulting quantum defect model not only reproduces nearly

all previous experimental observations, but also allows us to forecast spectra and dynamics in as-yet unobserved spectral regions.

II. EXPERIMENT

The energy levels included in this fit were drawn from double-resonance spectra that span the range $n^* = 5$, $v = 0$ (total energy $\sim 42500\text{ cm}^{-1}$) to $n^* = 20$, $v = 1$ (total energy $\sim 47500\text{ cm}^{-1}$). All spectra were analyzed using the techniques described in Ref. 29 and references therein. Although many of these levels have been reported previously,^{22,23,25,29,31} and the positions of some levels in the fit have been reconstructed using previously reported constants,²² most levels included in the fit were observed again in the present work at higher resolution and precision. A detailed list of all energy levels included in the fit appears in the online supplementary material.³²

In our experiments, Rydberg spectra of CaF are recorded using a two-chamber vacuum system, consisting of a laser ablation/molecular beam source (housed in the “source” chamber) and a time-of-flight mass spectrometer (housed in the “detection” chamber). A molecular beam of calcium monofluoride is produced in the source chamber by direct reaction of calcium plasma with fluoroform. A pulsed valve (General Valve, 0.5 mm diameter nozzle) emits a $350\text{ }\mu\text{s}$ pulse of 5% CHF_3 in He (30 psi stagnation pressure), which is synchronized with the pulsed production of a calcium plasma created by laser ablation of a rotating 1/4" diameter calcium rod by the third harmonic of a pulsed Nd:YAG laser (Spectra Physics GCR-130, 5–7 mJ per pulse at 355 nm). This produces a CaF molecular beam with a rotational temperature of $\sim 30\text{ K}$. The molecular beam is collimated by a 0.5 mm diameter conical skimmer placed between the source and detection chambers, and again by a 3.0 mm diameter skimmer prior to entering the laser excitation region of the detection chamber. Rydberg states are populated and ionized in the detection chamber by two colinear, pulsed laser beams that intersect the molecular beam at 90° . The CaF^+ ions that result are accelerated down the 75 cm flight tube of the mass spectrometer by a 250 V electric field pulse that arrives 200 ns after the pair of laser excitation pulses. Ions are detected by two microchannel plates arranged in a chevron configuration. The ion signals are amplified by a low-noise voltage amplifier and averaged over 40 shots (per dye laser frequency step) by a digital oscilloscope. The ion extraction assembly is contained within a Ni-plated shroud to isolate the excitation region from stray electric fields. Further details of the apparatus can be found in Ref. 31.

CaF Rydberg states lying between $n^* = 5$, $v = 0$ ($\sim 42500\text{ cm}^{-1}$) and the $v^+ = 0$ ionization limit (46998 cm^{-1}) are accessed by two-step excitation through the $\text{D}^2\Sigma^+$ intermediate state. Pump and probe laser pulses are produced by two pulsed dye lasers (Lambda Physik Scanmate 2E, pulse length $< 10\text{ ns}$, 0.1 cm^{-1} FWHM) both simultaneously pumped by the second harmonic of a single Nd:YAG laser (Spectra Physics GCR-290, injection-seeded, 400 mJ/pulse at 532 nm). The first

dye laser, operating with 4-dicyanomethylene-2-methyl-6-(*p*-dimethylaminostyryl)-4*H*-pyran (DCM) dye and equipped with a β -BBO frequency-doubling crystal, is tuned to a single rotational line of the $D^2\Sigma^+ \leftarrow X^2\Sigma^+$ transition. Due to unresolved spin structure, this apparently single rotational line terminates on two same-parity $J = N + 1/2$ and $J = N - 1/2$ levels. The second dye laser, typically operating with either pyridine 1 or DCM (output power $\sim 2\text{--}5$ mJ/pulse), is swept in frequency across the appropriate energy region and populates and photoionizes Rydberg states in a (1+1) REMPI scheme. The two laser pulses are partially overlapped in time to overcome an apparent rapid dissociation of the CaF Rydberg states into neutral atoms ($D_0^0 = 43500$ cm $^{-1}$). The frequencies of the pump and probe laser pulses are each calibrated using simultaneously recorded high-temperature (500 K) absorption spectra of molecular iodine.³³

CaF Rydberg states that lie above the $v^+ = 0$ ionization energy (total energy > 46998 cm $^{-1}$) are also accessed by two-step excitation through either the $D^2\Sigma^+$ or $F^2\Sigma^+$ intermediate states, with the apparatus configured exactly as above, but since all states spontaneously ionize in this energy region (a process which may be enhanced, or “forced”, by the 250 V extraction pulse in the mass spectrometer), spectra are recorded with the probe laser operating at a much lower output power (< 200 μ J/pulse) than the spectra at energies below the $v^+ = 0$ ionization threshold.

III. THEORY

Quantum defect theory goes beyond the Born–Oppenheimer approximation by invoking the BO approximation in the region of coordinate space in which the BO approximation is valid and applying a more appropriate physical picture elsewhere. Coordinate space is divided into three regions, according to the radial distance r between the Rydberg electron and the ion core center of charge: a “core” region, a “Born–Oppenheimer” region, and an “asymptotic” region. The core region is the innermost volume, bounded by a hypothetical radius r_c , inside which the Rydberg electron experiences strong short-range electrostatic interactions with the core particles. The Born–Oppenheimer region includes and extends beyond the core region and is bounded by another hypothetical radius $r_{\text{BO}} > r_c$. In the BO region, the motion of the Rydberg electron is faster than the motion of the nuclei, and the BO approximation is approximately valid. Rydberg states approximately conform to the BO approximation if the bulk of the Rydberg electron probability density lies within the BO region. Finally, the asymptotic region extends from the core boundary out to infinite electron-ion separation ($r_c < r$). Importantly, the BO region overlaps the innermost portion of the asymptotic region. In the asymptotic region, the interactions between the Rydberg electron and core particles are weak and dominated by the long-range Coulomb interaction. Although the Rydberg electron probability density lies almost entirely in the asymptotic region for all Rydberg states, non-Born–Oppenheimer effects only become important for states in which the electron probability density lies significantly outside the BO region. In QDT,

the only explicit knowledge required about the behavior of the electron wavefunction within the core region is that the collision with the core results in a phase shift of the Rydberg electron wavefunctions outside the core region. The molecular wave functions are only explicitly considered outside the core and are expressed differently in the BO and asymptotic regions.

In the asymptotic region, the Rydberg electron only interacts with the ion-core at long range, and consequently, the motions of the Rydberg electron and ion-core are approximately separable. In this region, the molecular Hamiltonian is divided into ion-core, Rydberg electron, and interaction terms:

$$\begin{aligned}\hat{H} &= \hat{H}^0 + \hat{H}^1, \\ \hat{H}^0 &= \hat{H}_{\text{ion}} + \hat{H}_{\text{Coulomb}}, \\ \hat{H}^1 &= \hat{H}_{\text{residual}}.\end{aligned}\quad (2)$$

Here, \hat{H}_{ion} represents the full Hamiltonian of the CaF $^+$ ion-core, \hat{H}_{Coulomb} describes the motion of the excited electron in the Coulomb field of the ion-core, and $\hat{H}_{\text{residual}}$ represents all of the interactions between the electron and the ion-core beyond the simple Coulomb attraction. If the only interaction between the electron and the ion core were the long-range Coulomb interaction (i.e., if $\hat{H}^1 = \hat{H}_{\text{residual}} = 0$), the eigenfunctions of the system would be the eigenfunctions of the zero-order Hamiltonian \hat{H}^0 . In a real diatomic molecule, there are always short- and long-range nonspherically symmetric interactions between the electron and the ion, and thus \hat{H}^1 is always nonvanishing in a real system. The nonsphericity of the interactions contained in \hat{H}^1 causes interactions between the angular motion of the Rydberg electron and the rotational motion of the core (mixing of the ℓ and N^+ quantum numbers), and the internuclear distance dependence of \hat{H}^1 couples the Rydberg electron with the vibrational motion of the core (mixing of n and v^+).

In the asymptotic region, the zero-order Hamiltonian \hat{H}^0 is used as a starting point to define a set of “channel functions” (which play a role similar to the basis set of an effective Hamiltonian), and the interaction term \hat{H}^1 causes interactions between the channels and mixing of the channel functions. A channel wavefunction of the electron-ion system is specified by the vibration-rotation v^+, N^+ state of the ion-core, the orbital angular momentum of the Rydberg electron, ℓ , the total angular momentum of the molecule exclusive of spin, N , and parity index p ($p = 0$ for positive parity; $p = 1$ for negative parity) as

$$\begin{aligned}\psi_{\ell v^+ N^+}^{(N,p)}(E, r, R, \Omega) &= \sum_{\ell' v'^+ N'^+} \{ f_\ell(\varepsilon_{v^+ N^+}, r) \delta_{\ell v^+ N^+, \ell' v'^+ N'^+} \\ &\quad - K_{\ell v^+ N^+, \ell' v'^+ N'^+}^{(rv)}(E) g_{\ell'}(\varepsilon_{v'^+ N'^+}, r) \} \\ &\quad \times \chi_{v'^+}^{(N^+)}(R) \Phi_{\ell' N'^+}^{(N,p)}(\Omega).\end{aligned}\quad (3)$$

Each possible combination of the quantum numbers ℓ , N^+ , N , and v^+ constitutes a separate channel. The term in

brackets is the radial part of the wavefunction of the Rydberg electron (radial coordinate r and binding energy $\varepsilon_{v^+N^+} = E - E_{v^+N^+,\infty}$, where $E_{v^+N^+,\infty}$ are the rovibrational energy levels of the CaF^+ ion core; $\varepsilon_{v^+N^+} < 0$ for closed channels), $\Phi_{\ell N^+}^{(N,p)}$ represents the angular part of the Rydberg electron and core rotational wavefunctions (angular coordinates Ω) coupled to form eigenfunctions of \mathbf{N}^2 , and $\chi_{v^+}^{(N^+)}(R)$ is the vibrational wavefunction of the ion-core. The product form of these functions reflects the division of the Hamiltonian of Eq. (2) into electron, ion, and interaction parts. The “rovibronic” (super-script “rv”) reaction matrix, $\mathbf{K}^{(\text{rv})}$ [elements of which appear as coefficients of the irregular Coulomb function, g , in Eq. (3)], describes the mixing of the channels due to the interactions contained in \hat{H}^1 . (The reaction matrix and associated quantities are described in Appendix A 0 1.) Because the outcome of any electron-ion scattering event depends on the kinetic energy of the incoming electron, the rovibronic reaction matrix $\mathbf{K}^{(\text{rv})}$ is energy-dependent. Here we evaluate the matrix elements $K_{\ell v^+N^+, \ell' v'^+N'^+}^{(\text{rv})}(E)$ in an energy-modified adiabatic approximation of the type introduced by Nesbet³⁴ by setting $E - E_{v^+N^+,\infty} = \bar{\varepsilon}_{v^+N^+, v'^+N'^+} = (\varepsilon_{v^+N^+} + \varepsilon_{v'^+N'^+})/2$. The total wavefunction of the molecule is expressed as a superposition of channel functions,

$$\Psi_{r>r_c}^{(N,p)}(E) = \sum_{\ell v^+N^+} B_{\ell v^+N^+}^{(N,p)}(E) \psi_{\ell v^+N^+}^{(N,p)}(E), \quad (4)$$

where the coefficients, $B_{\ell N^+ v^+}$, called channel mixing amplitudes describe the contributions of each channel to the molecular wavefunctions, i.e., the amplitude of the system in each channel for a given total energy E .

If all of its indices are treated independently, the dimension of the rovibronic reaction matrix, $\mathbf{K}^{(\text{rv})}$, is quite large. In a typical calculation for a single value of total angular momentum, N , that includes channels with $\ell \leq 3$, $v^+ \leq 5$, and all accessible rotational channels ($N^+ = |N - \ell| \cdots (N + \ell)$), $\mathbf{K}^{(\text{rv})}$ will have up to 60 rows and columns, resulting in a total of up to $n(n + 1)/2 = 1830$ independent elements. Such a large number of independently adjustable fit parameters would make a direct fit to the spectrum based on the $\mathbf{K}^{(\text{rv})}$ matrix impossible.

The central simplification^{10,11} of QDT that makes this problem tractable is the fact that, in the Born–Oppenheimer region, the motions of *all* electrons are instantaneous with respect to the nuclei. In the BO region, it is therefore physically appropriate to define a set of channel functions which are expressed as BO products:

$$\psi_{v\Lambda}^{(\text{BO}, N, p)} = \phi_\Lambda \chi_v^{(N)} \Phi_{NM}, \quad (5)$$

where here ϕ_Λ , $\chi_v^{(N)}$, and Φ_N are the electronic, vibrational, and rotational wavefunctions of the neutral molecule, respectively. Since the BO region extends beyond the core region, ($r > r_c$) the electronic wavefunction of the molecule

is further separable into Rydberg electron and ion-core factors:

$$\begin{aligned} \psi_{v\Lambda}^{(\text{BO}, N, p)}(E) = & \left\{ \sum_\ell b_{\ell\Lambda}(R, \varepsilon) \left[f(\varepsilon, r) \cos \pi \mu_\alpha^{(\Lambda)}(R, \varepsilon) \right. \right. \\ & \left. \left. - g(\varepsilon, r) \sin \pi \mu_\alpha^{(\Lambda)}(R, \varepsilon) \right] Y_{\ell\lambda}(\theta, \phi) \right\} \\ & \times \phi_{\Lambda^+}(\eta) \chi_v^{(N)}(R) \Phi_{NM}(\Theta, \Phi) \end{aligned} \quad (6)$$

Here, the term in braces is the wavefunction of the Rydberg electron, $\phi_{\Lambda^+}(\eta)$ is the electronic wavefunction of the ion-core (electronic coordinates η), and $\chi_v^{(N)}(R)$ and $\Phi_{NM}(\Theta, \Phi)$ are the vibrational and rotational wave functions of the neutral molecule. The coefficients $b_{\ell\Lambda}(R, \varepsilon)$ describe the orbital angular momentum character of the electronic wavefunction of the Rydberg electron, and the $\mu_\alpha^{(\Lambda)}(R, \varepsilon)$ are the “eigenquantum defects”. The eigenquantum defects (discussed in Appendix A) are the quantum defects of the nonrotating molecule and can be determined approximately from the BO potential energy curves of the lowest electronic states by inversion of the Rydberg formula. A general wave function of the molecule can be expressed as a sum of BO products:

$$\Psi_{r>r_c}^{(\text{BO}, N)}(E) = \sum_{v\Lambda} A_{v\Lambda}^{(N)}(E) \psi_{v\Lambda}^{(\text{BO}, N)}(E). \quad (7)$$

Since the asymptotic region *contains* the outer BO region, the two forms of the full molecular wave function [Eqs. (4) and (7)] must be equal in the outer part of the BO region. By equating them, it is possible to derive a relationship called the “frame transformation”^{10–12,14,15} that expresses each element of the large $\mathbf{K}^{(\text{rv})}$ matrix in terms of a much smaller number of purely electronic quantum defect matrix elements:

$$\begin{aligned} K_{\ell, v^+, N^+; \ell', v'^+, N'^+}^{(\text{rv})}(E) = & \sum_\Lambda \langle \Lambda | N^+ \rangle^{(N, \ell, p)} \langle N'^+ | \Lambda \rangle^{(N', \ell', p)} \\ & \times \left[\int \chi_{v^+}^{(N^+)}(R) K_{\ell, \ell'}^{(\text{el})(\Lambda)}(R, \bar{\varepsilon}_{v^+N^+, v'^+N'^+}) \chi_{v'^+}^{(N'^+)}(R) dR \right]. \end{aligned} \quad (8)$$

Matrix elements of the rovibronic reaction matrix $\mathbf{K}^{(\text{rv})}$ are thus expressed in terms of the known ion-core vibrational wave functions, $\chi_{v^+}^{(N^+)}(R)$, known angular momentum coupling coefficients, $\langle \Lambda | N^+ \rangle^{(N, \ell, p)}$,³⁵

$$\begin{aligned} \langle \Lambda | N^+ \rangle^{(N, \ell, p)} = & (-1)^{N-\Lambda} \left[\frac{1 + (-1)^{p-N^++\ell}}{2} \right] \\ & \times \left[\frac{2}{(1 + \delta_{\Lambda 0})} \right]^{1/2} (2N^+ + 1)^{1/2} \\ & \times \binom{N^+ \ \ell \ N}{0 \ \ \Lambda - \Lambda}, \end{aligned} \quad (9)$$

and a relatively small number of *purely electronic* (superscript “el”) reaction matrix elements, $K_{\ell\ell'}^{(\text{el})(\Lambda)}(R, \varepsilon)$. The superscript p in the $\langle A|N^+ \rangle^{(N, \ell, p)}$ coefficients indexes the total parity $P = (-1)^{\ell+N^+}$ of the given channel ($p = 0$ for positive total parity and $p = 1$ for negative total parity).

The electronic reaction matrix, $\mathbf{K}^{(\text{el})}$, forms the heart of the quantum defect model. It expresses the effect of all non-Coulomb interactions on the electronic wavefunctions of the neutral molecule for small radial distances r , where the motions of *all* electrons are fast relative to the nuclei and the Born–Oppenheimer approximation is valid. The frame transformation of Eq. (8) transforms this Born–Oppenheimer picture to the separated electron/ion picture embodied in Eqs. (2)–(4), which is more appropriate at large r (i.e., for the electron at long range). Thus, this frame transformation describes all possible departures from Born–Oppenheimer behavior. The matrix elements of $\mathbf{K}^{(\text{el})}$ can be equivalently expressed in terms of the quantum defect matrices $\boldsymbol{\mu}$ or $\bar{\boldsymbol{\mu}}$ (see Appendix A). The matrix elements $K_{\ell\ell'}^{(\text{el})(\Lambda)}(R, \varepsilon)$ are given in terms of $\boldsymbol{\mu}$ by

$$K_{\ell\ell'}^{(\text{el})(\Lambda)}(R, \varepsilon) = \tan \pi \mu_{\ell\ell'}^{(\Lambda)}(R, \varepsilon). \quad (10)$$

Since the electronic reaction matrix, $\mathbf{K}^{(\text{el})}$, that appears in Eqs. (5) and (10) describes the scattering of the electron from the ion-core at short range (in the region of space where the electron moves fast enough that the nuclei are effectively fixed in space and the Born–Oppenheimer approximation is valid), $\mathbf{K}^{(\text{el})}$ is parametrically dependent on R and ε and is diagonal in Λ . Since the interaction between the Rydberg electron and the polar ion-core is strongly anisotropic, $\mathbf{K}^{(\text{el})}$ is nondiagonal in the orbital angular momentum quantum number, ℓ . The frame transformation of Eq. (8) reduces the number of parameters required to represent the system from greater than 1000 to a few tens of quantum defect parameters, $\mu_{\ell\ell'}^{(\Lambda)}(R, \varepsilon)$, or $\bar{\mu}_{\ell\ell'}^{(\Lambda)}(R, \varepsilon)$.

As discussed in Ref. 36, the frame transformation expression [Eq. (8)] is only valid when the interaction between the electron and the ion core is “sudden”; the nuclei must not have time to rotate or vibrate while the electron is inside the core. The Born–Oppenheimer approximation must be valid across the entire core region. The core boundary lies at a radius, r_c , beyond which all non-Coulomb electrostatic interactions are much weaker than the Coulomb interaction and can be neglected. In a polar molecule such as CaF, the longest-range non-Coulomb interaction is due to the dipole field of the core. Thus, at the core boundary we must have

$$\frac{2Z\mathfrak{N}}{r_c} = x \frac{2Q_1\mathfrak{N}}{r_c^2}, \quad (11)$$

where Z is the charge of the ion-core, Q_1 is the electric dipole moment of the core, and $x \gg 1$. Both sides of (11) are expressed in cm^{-1} . Equation (11) defines the core radius $r_c = x Q_1 / Z$. In order for the collision to be impulsive, the Coulomb energy at r_c must be far greater than the ion-core

internal energy level spacings. For rotation, this implies that

$$\frac{2Z\mathfrak{N}}{r_c} = y 2B(N^+ + 1), \quad (12)$$

and for vibration,

$$\frac{2Z\mathfrak{N}}{r_c} = z\omega. \quad (13)$$

For the collision to be impulsive, both $y \gg 1$ and $z \gg 1$. Setting $x = 10$ (i.e., defining r_c as the radius at which the Coulomb field is ten times stronger than the dipole field), with $Q_1 = 3.5 \text{ e a}_0$, $B = 0.37 \text{ cm}^{-1}$, and $\omega = 694 \text{ cm}^{-1}$ for CaF^+ , and setting $N^+ = 15$ (the highest rotational channel considered in this analysis), gives $r_c = 35 \text{ a}_0$, $y = 565$, and $z = 9$. We thus see that the collision is impulsive with respect to rotation, and still fast with respect to vibration.

For comparison, we can derive similar suddenness parameters for H_2 , where the frame transformation has been successfully used to describe the rotational^{10,37} and vibrational^{37,38} structure of Rydberg states. Since H_2 has no electric dipole moment, the longest-range non-Coulomb interaction is due to the quadrupole field of the ion core. Thus, at the core boundary,

$$\frac{2\mathfrak{N}Z}{r_c} = x \frac{2\mathfrak{N}Q_2}{r_c^3}, \quad (14)$$

where Q_2 is the electric quadrupole moment of the core and $x \gg 1$, giving a core radius $r_c = \sqrt{xQ/Z}$. In H_2^+ , $Q_2 = 1.53 \text{ e a}_0^2$, $B = 30.2 \text{ cm}^{-1}$, and $\omega = 2322 \text{ cm}^{-1}$.^{36,39} Setting $x = 10$ and $N^+ = 6$ (the highest rotational channel considered in³⁷) gives $r_c = 3.9 \text{ a}_0$, $y = 155$, and $z = 24$. The collision is again clearly impulsive with respect to rotation, but somewhat faster with respect to vibration in H_2 than for CaF. The frame transformation should be valid for both molecules; however, the Born–Oppenheimer region will extend further beyond the core region for H_2 than for CaF.

It is important to emphasize that the electronic reaction matrix, $\mathbf{K}^{(\text{el})}$, or equivalently the quantum defect matrices, $\boldsymbol{\mu}$ and $\bar{\boldsymbol{\mu}}$, may be viewed as a “clamped nuclei” representation of the *global* rovibronic structure of the molecule, which is more powerful and inclusive than the “clamped nuclei” approximation by which each *local* adiabatic potential energy curve is defined. It is a near-universal misconception to view Rydberg states as incompatible with the Born–Oppenheimer approximation. In fact, quantum defect theory is built on a Born–Oppenheimer picture, but *for all electronic states at once* rather than *one electronic state at a time*.

Energy levels of the molecule are located by demanding that the bound state wavefunctions [Eq. (4)] vanish at infinite electron-ion separation. This requirement results in a homogeneous linear system of equations that involves the symmetric rovibronic reaction matrix, $\mathbf{K}^{(\text{rv})}$, and the channel mixing amplitudes, \mathbf{B} ,

$$\begin{aligned} \mathbf{K}^{(\text{rv})}\mathbf{B} &= -\mathbf{P}(E)\mathbf{B}, \text{ i.e.,} \\ [\mathbf{P}(E) + \mathbf{K}^{(\text{rv})}]\mathbf{B} &= 0. \end{aligned} \quad (15)$$

$\mathbf{P}(E)$ is the diagonal “phase matrix”:³⁰

$$\mathbf{P}(E) = \begin{pmatrix} \tan \pi v_{v^+N^+} & 0 & 0 & 0 & 0 & 0 & 0 & 0 \\ 0 & \tan \pi v_{v^+N^++1} & 0 & 0 & 0 & 0 & 0 & 0 \\ 0 & 0 & \tan \pi v_{v^+N^++2} & 0 & 0 & 0 & 0 & 0 \\ 0 & 0 & 0 & \dots & 0 & 0 & 0 & 0 \\ 0 & 0 & 0 & 0 & \tan \pi v_{v^++1,N^+} & 0 & 0 & 0 \\ 0 & 0 & 0 & 0 & 0 & \tan \pi v_{v^++1,N^++1} & 0 & 0 \\ 0 & 0 & 0 & 0 & 0 & 0 & \tan \pi v_{v^++1,N^++2} & 0 \\ 0 & 0 & 0 & 0 & 0 & 0 & 0 & \dots \end{pmatrix}, \quad (16)$$

where $\pi v_{v^+N^+} = \pi \sqrt{-\mathfrak{R}/\varepsilon} = \pi \sqrt{\mathfrak{R}/(E_{v^+N^+,\infty} - E)}$, with ε and E in cm^{-1} . Energy levels exist at the values of E where the determinant of the coefficient matrix vanishes:

$$\det [\mathbf{P}(E) + \mathbf{K}^{(\text{rv})}(E)] = 0, \quad (17)$$

and a set of channel mixing amplitudes can be found for each value of E that satisfies Eq. (17).

Within the scope of the experimental observations to date, only one important effect is missing from this quantum defect model: dissociation to neutral atoms. As discussed in Sec. I, there are two dissociative covalent states [configuration $\text{Ca}^0(4s^2)\text{F}^0(2p^5)$, giving rise to one ${}^2\Sigma^+$ state and one ${}^2\Pi$ state], the potential energy curves of which intersect the Rydberg states converging to the $X^1\Sigma^+$ ground state of the CaF^+ ion-core (configuration Ca^{2+}F^- ; doubly closed-shell). These intersections give rise to normal predissociation of the Rydberg states and also cause intensity anomalies in the photoionization spectra and are expected to affect photoionization pathways and branching ratios.⁴⁰ However, the omission of interactions with these repulsive states does not diminish the utility of this quantum defect model, either as a compact representation of the rich energy level structure or as a tool for understanding level patterns, dynamics, and mechanism. None of these effects significantly alters the positions of the energy levels observed here, and while the presence of the dissociation continua may give rise to additional effects beyond the predictions of our model, this model remains a useful tool with great capacity for understanding molecular Rydberg states. It should be noted that the theoretical apparatus for including the effects of one or more dissociation continua does exist,^{41,42} and represents a logical next step for our analysis of CaF .

IV. RESULTS AND DISCUSSION

A. Application to CaF

In the fit, we include nearly all observed electronic states of CaF in each of the ten “s” [Σ], “p” [Σ, Π], “d” [Σ, Π, Δ],

and “f” [$\Sigma, \Pi, \Delta, \Phi$] Rydberg series⁴³ with $5 \leq n* \leq 20$. The input data set spans approximately 5000 cm^{-1} , includes levels with $0 \leq v \leq 3$ and $0 \leq N \leq 12$, and encompasses a wide range of dynamical phenomena. At the low-energy end of the spectral range, the Born–Oppenheimer approximation is almost valid, and rotation-vibration energy levels are organized as separate electronic states with regular rotational structure. The levels then pass through an energy region in which numerous vibronic interactions occur, where the rotational structure is mostly regular but levels are displaced from their expected positions by electronic-vibrational perturbations. Finally, at the high-energy end of the spectral range, the $n \rightarrow n+1$ electronic spacing becomes sufficiently narrow that $\Delta v \neq 0$ interactions remain localized, but electronic-rotational interactions become so strong that the regular rotational structure becomes hopelessly shattered and separate “electronic states” cease to exist. Even though all of the input data are affected by nonadiabatic interactions, our quantum defect model represents all spectroscopic data very well.

In the quantum defect fit model we include channels with $0 \leq \ell \leq 3$, $0 \leq v^+ \leq 3$, and $0 \leq N \leq 12$. For this range of quantum numbers and the restrictions imposed by the addition of angular momentum, $\mathbf{N} = \ell + \mathbf{N}^+$, and total parity, $p = (-1)^{\ell+N^+}$, each vibrational channel consists of ten rotational channels with positive rotationless (N -independent) parity $p' = (-1)^{N+\ell+N^+}$ and six with negative rotationless parity for each value of $N \geq 3$. (Note that because of the restriction imposed by the angular momentum addition $\mathbf{N} = \ell + \mathbf{N}^+$, some rotational channels do not exist for $N < 3$.) In all, our model includes a total of 60 channels of positive rotationless parity and 36 channels of negative rotationless parity for $N \geq 3$.

To facilitate the fitting procedure, we have employed the $\bar{\mu}$ defects,^{30,38} as the primary fitted parameters rather than the more standard μ defects. As discussed in Refs. 38 and 30, use of the $\bar{\mu}$ quantum defects results in a smoother dependence of the electronic reaction matrix $\mathbf{K}^{(\text{el})}$ on the internuclear distance R . The relationship between the μ and $\bar{\mu}$ defects is discussed in Appendix A.

In the fit, we allow the fitted quantum defect parameters to vary linearly and quadratically with both R and ε . The quantum defects are expanded about the equilibrium internuclear distance R_e^+ and the ionization threshold, $\varepsilon = 0$, according to

$$\begin{aligned} \bar{\mu}_{\ell\ell'}^{(A)}(R, \varepsilon) \equiv & \bar{\mu}_{\ell\ell'}^{(A)} \Big|_{R=R_e^+; \varepsilon=0} + \frac{\partial \bar{\mu}_{\ell\ell'}^{(A)}}{\partial R} \Big|_{R=R_e^+; \varepsilon=0} (R - R_e^+) + \frac{1}{2} \frac{\partial^2 \bar{\mu}_{\ell\ell'}^{(A)}}{\partial R^2} \Big|_{R=R_e^+; \varepsilon=0} (R - R_e^+)^2 \\ & + \frac{\partial \bar{\mu}_{\ell\ell'}^{(A)}}{\partial \varepsilon} \Big|_{R=R_e^+; \varepsilon=0} \cdot \varepsilon + \frac{1}{2} \frac{\partial^2 \bar{\mu}_{\ell\ell'}^{(A)}}{\partial \varepsilon^2} \Big|_{R=R_e^+; \varepsilon=0} \cdot \varepsilon^2 \\ & + \frac{\partial^2 \bar{\mu}_{\ell\ell'}^{(A)}}{\partial \varepsilon \partial R} \Big|_{R=R_e^+; \varepsilon=0} (R - R_e^+) \cdot \varepsilon \end{aligned} \quad (18)$$

The quantum defect matrix elements and their derivatives with respect to R and ε are taken as adjustable parameters and are allowed to vary in a carefully controlled way during the fit process.

B. Fit procedure

Although the fitting process makes use of standard fitting techniques, the complexity of the model and the nonlinear and correlated influences of parameters on the energy levels demand a careful, iterative approach. A full set of *ab initio* quantum defect derivatives was not available at the commencement of the fit, so it was not possible to initialize the fit using plausible estimates of many of the quantum defect derivatives. We therefore developed a strategy whereby we could incrementally add a small number of necessary adjustable parameters to the model, while at the same time maintaining confidence that the fitted parameters remain physically reasonable.

Our overall strategy is to begin fitting the model starting with the $\bar{\mu}_{\ell\ell'}^{(A)}|_{R_e^+}$ and $\partial \bar{\mu}_{\ell\ell'}^{(A)}/\partial R$ quantum defect parameters and ion-core spectroscopic constants ($T_\infty(v^+ = 0, N^+ = 0)$, ω_e^+ , $\omega_e x_e^+$, B_e^+ , D_e^+ , α_e^+) determined from a previous fit³⁰ to spectral data that spanned a much narrower range of energy (47000–47300 cm⁻¹ in Ref. 30, compared with 42600–47400 cm⁻¹ here), and gradually increase the number of adjustable quantum defect derivatives. Our procedure consisted of four main steps: (i) initialization and convergence using $\bar{\mu}_{\ell\ell'}^{(A)}|_{R_e^+}$ and $\partial \bar{\mu}_{\ell\ell'}^{(A)}/\partial R$ parameters determined in Ref. 30, (ii) division of the fit into two parts which are fitted separately, to obtain estimates for $\partial \bar{\mu}_{\ell\ell'}^{(A)}/\partial \varepsilon$, (iii) convergence of fit using $\bar{\mu}_{\ell\ell'}^{(A)}|_{R_e^+}$ and $\partial \bar{\mu}_{\ell\ell'}^{(A)}/\partial R$, and $\partial \bar{\mu}_{\ell\ell'}^{(A)}/\partial \varepsilon$ parameters, and (iv) addition of any necessary quadratic derivatives, i.e., $\partial^2 \bar{\mu}_{\ell\ell'}^{(A)}/\partial R^2$, $\partial^2 \bar{\mu}_{\ell\ell'}^{(A)}/\partial \varepsilon^2$, and $\partial^2 \bar{\mu}_{\ell\ell'}^{(A)}/\partial \varepsilon \partial R$. Although we attempted to allow the spectroscopic constants of the ion core to vary during each of the four main steps, no substantial improvement in fit quality ever resulted, and the ion-core constants were therefore taken as constant and remained at the

values given in Ref. 30 throughout the duration of the fit process.

All four steps of the fit are conducted using the “robust” linear least-squares fit method.⁴⁴ This is a weighted fit method in which weight factors are assigned to the observed energy levels in proportion to their agreement with the calculated levels: weight factors are largest for levels with the smallest residuals and decrease rapidly as the residuals exceed the standard deviation of the fit. The robust method is absolutely essential to the work we describe here, since it allows us to continuously expand the fit by adding both new observed energy levels and new adjustable fit parameters, while assuring that the well-fit levels and well-determined fit parameters already included are never compromised.

The fit process is also, at nearly every step, partially combinatorial. Our goal is to achieve an optimal fit by incrementally adding the smallest number of new adjustable parameters possible. Although we guide this process at every step using physical intuition to the maximum extent possible, it is difficult to gauge the effect of adjusting any given quantum defect parameter (or set of parameters) because their effects on the energy level structure are not perfectly separable from one another across the entire energy range. This is partially due to the large number of off-diagonal ($\Delta v \neq 0$, $\Delta \Lambda \neq 0$, $\Delta \ell \neq 0$, etc.) interactions sampled in the fit. For example, while the $\bar{\mu}_{\ell\ell'}^{(\Sigma)}|_{R_e^+}$ parameters are nearly decoupled from the $\bar{\mu}_{\ell\ell'}^{(\Pi)}|_{R_e^+}$ parameters at low n^* , the two sets of parameters do become somewhat correlated at high n^* as Rydberg states of Σ and Π symmetry become mixed by ℓ -uncoupling interactions. Other sets of fit parameters are strongly correlated by definition: any given $\partial \bar{\mu}_{\ell\ell'}^{(A)}/\partial \varepsilon$ derivative and its associated $\partial^2 \bar{\mu}_{\ell\ell'}^{(A)}/\partial \varepsilon^2$ derivative, for example, will have some similar effects on the energy level structure far from the ionization threshold. We sidestep these issues by simply adjusting (at every iteration of the fit) many different combinations of parameters, determining which combinations result in significant improvement in the fit, and feeding the output to the next iteration. Although each iteration of the fit takes several hours to complete, multiprocessor computation makes this process feasible

and allows us to extend the fit in several different directions simultaneously.

1. Initialization and convergence using $\bar{\mu}_{\ell\ell'}^{(\Lambda)}|_{R_e^+}$ and $\partial\bar{\mu}_{\ell\ell'}^{(\Lambda)}/\partial R$

The first step of our procedure is to fit all observed energy levels starting with the $\bar{\mu}_{\ell\ell'}^{(\Lambda)}|_{R_e^+}$ and $\partial\bar{\mu}_{\ell\ell'}^{(\Lambda)}/\partial R$ parameters determined in Ref. 30. While it was apparent that this limited set of fit parameters (20 $\bar{\mu}_{\ell\ell'}^{(\Lambda)}|_{R_e^+}$ and 20 $\partial\bar{\mu}_{\ell\ell'}^{(\Lambda)}/\partial R$) could never yield perfect correspondence between the quantum defect model and the experimental data, some refinement of the parameters (from their values in Ref. 30) was to be expected, especially for the $\partial\bar{\mu}_{\ell\ell'}^{(\Lambda)}/\partial R$ derivatives. The levels in the expanded data set cover a wider range of vibrational quantum numbers and participate in a greater number of $\Delta\nu \neq 0$ perturbations, both of which should afford greater sensitivity to the dependence of the quantum defects on R .

We initially varied each $\bar{\mu}_{\ell\ell'}^{(\Lambda)}|_{R_e^+}$ and $\partial\bar{\mu}_{\ell\ell'}^{(\Lambda)}/\partial R$ parameter, *one at a time*, in a combinatorial manner to identify those parameters in particular need of refinement. When a poorly fit parameter was identified and when subsequent adjustment of this parameter significantly improved the fit quality, it was allowed to vary and its optimum value was taken for use in the next fit iteration. Generally, adjustment of $\bar{\mu}$ matrix elements that are diagonal in ℓ had the largest impact on the fit quality. This process was repeated until it was no longer possible to improve the quality of the fit by adjusting the value of one parameter at a time. The procedure was then repeated using combinations of parameters, typically as the following:

- One $\bar{\mu}_{\ell\ell'}^{(\Lambda)}|_{R_e^+}$ parameter and its associated $\partial\bar{\mu}_{\ell\ell'}^{(\Lambda)}/\partial R$ derivative.
- Two different diagonal $\bar{\mu}_{\ell\ell'}^{(\Lambda)}|_{R_e^+}$ parameters with the same value of Λ .
- Two different diagonal $\bar{\mu}_{\ell\ell'}^{(\Lambda)}|_{R_e^+}$ parameters with the same value of Λ as well as the off-diagonal matrix element between them, i.e., $\bar{\mu}_{ss}^{(\Sigma)}|_{R_e^+}$, $\bar{\mu}_{pp}^{(\Sigma)}|_{R_e^+}$, and $\bar{\mu}_{sp}^{(\Sigma)}|_{R_e^+}$.
- Combinations of parameters as in c), plus their $\partial\bar{\mu}_{\ell\ell'}^{(\Lambda)}/\partial R$ derivatives.
- All $\bar{\mu}_{\ell\ell'}^{(\Lambda)}|_{R_e^+}$ matrix elements for a given Λ .
- All $\bar{\mu}_{\ell\ell'}^{(\Lambda)}|_{R_e^+}$ and $\partial\bar{\mu}_{\ell\ell'}^{(\Lambda)}/\partial R$ matrix elements for a given value of Λ .

Strong attempts were made to ensure that the smallest possible number of parameters was varied at each step and that this condition was met. We typically attempted to vary 5–20 combinations of parameters at *each of the above steps*.

2. Generation of estimates of $\partial\bar{\mu}_{\ell\ell'}^{(\Lambda)}/\partial\epsilon$

After the initial refinement of the fit parameters, according to the procedure described in Sec. IV B 1, it became apparent that the energy dependence of the quantum defects would need to be considered as well. To generate estimates of the derivatives of the quantum defects with respect to energy, $\partial\bar{\mu}_{\ell\ell'}^{(\Lambda)}/\partial\epsilon$, we divided the fit into two halves: states with $n^* = 5$ –10 in the “low energy” half, and states with n^*

= 10–20 in the “high energy” half. Each half was then subject to the procedure described in Sec. IV B 1. This generated two sets of converged fit constants, from which initial estimates of each $\partial\bar{\mu}_{\ell\ell'}^{(\Lambda)}/\partial\epsilon$ could be obtained by assuming a linear dependence on energy, *i.e.*, $\partial\bar{\mu}_{\ell\ell'}^{(\Lambda)}/\partial\epsilon|_{\text{est.}} = (\bar{\mu}_{\ell\ell'}^{(\Lambda)}|_{\text{high}} - \bar{\mu}_{\ell\ell'}^{(\Lambda)}|_{\text{low}})/\Delta\bar{\epsilon}$.

3. Convergence using $\bar{\mu}_{\ell\ell'}^{(\Lambda)}|_{R_e^+}$, $\partial\bar{\mu}_{\ell\ell'}^{(\Lambda)}/\partial R$, and $\partial\bar{\mu}_{\ell\ell'}^{(\Lambda)}/\partial\epsilon$

After initial estimates were obtained for the energy derivatives, $\partial\bar{\mu}_{\ell\ell'}^{(\Lambda)}/\partial\epsilon$, according to Sec. IV B 2, the data were again subject to an iterative fit procedure similar to steps (a)–(f) in Sec. IV B 1. In this stage of the fit procedure, the energy derivatives were varied as well as the $\partial\bar{\mu}_{\ell\ell'}^{(\Lambda)}/\partial R$ derivatives, and as before, new values for the fit parameters were selected by adjusting the most effective combinations of the smallest number of fit parameters, until all parameters were fully converged.

4. Refinement by addition of second derivatives:

$\partial^2\bar{\mu}_{\ell\ell'}^{(\Lambda)}/\partial R^2$, $\partial^2\bar{\mu}_{\ell\ell'}^{(\Lambda)}/\partial\epsilon^2$, and $\partial^2\bar{\mu}_{\ell\ell'}^{(\Lambda)}/\partial\epsilon\partial R$

Following the convergence of the fit in Sec. IV B 3, a carefully selected subset of the $\partial^2\bar{\mu}_{\ell\ell'}^{(\Lambda)}/\partial R^2$, $\partial^2\bar{\mu}_{\ell\ell'}^{(\Lambda)}/\partial\epsilon^2$, and $\partial^2\bar{\mu}_{\ell\ell'}^{(\Lambda)}/\partial\epsilon\partial R$ derivatives was added to improve the fit quality for the very lowest ($n^* \approx 5$) Rydberg states. These second derivatives were adjusted, one at a time, to identify those few parameters that would be most effective in improving the quality of the fit. As it was not possible to generate empirical estimates of the values of the second derivatives by any method, each parameter was adjusted with its initial value taken to be zero. Following the identification of the most important second derivatives, combinations of these parameters were adjusted in a scheme similar to that outlined in steps (a)–(f) of Sec. IV B 1. Only a few second derivatives were introduced, primarily in diagonal elements for Σ and Π symmetries.

After these second derivatives had been added, all parameters were varied together for several iterations until convergence. Once all parameters had converged, the fit was considered complete, as the addition of more parameters would impart undue flexibility to the fit model and possibly result in physically unrealistic values.

The amount of computational time required to achieve an optimal fit is noteworthy. Because of the large number of energy levels included in the fit, each iteration (i.e., each trial combination of fit parameters) required between 30 min and 10 h of computation time, depending on the number of parameters varied. Even using computers with eight or more processors, the entire fitting process took more than a year of continuous computation to complete.

C. Quantum defect matrices and quality of fit

The $\bar{\mu}^{(\Lambda)}$ quantum defect parameters obtained from the fit are shown in Table I. Uncertainties (1Σ) are indicated in parentheses. From our fit, it was possible to reliably determine the values of nearly all of the $\bar{\mu}_{\ell\ell'}^{(\Lambda)}|_{R_e^+}$ matrix elements, nearly

TABLE I. $\bar{\mu}$ quantum defect matrix element values and derivatives obtained from fits to CaF Σ , Π , Δ , and Φ states. Uncertainties are indicated in parentheses. If no numerical value is given, the parameter has been held fixed at zero.

$\mu(R_e^+, \varepsilon = 0)$	$\partial\mu/\partial R[a_0^{-1}]$	$\partial\mu/\partial E[\text{Ry}^{-1}]$	$\partial^2\mu/\partial R^2[a_0^{-2}]$	$\partial^2\mu/\partial E^2[\text{Ry}^{-2}]$	$\partial^2\mu/\partial E\partial R[\text{Ry}^{-1}a_0^{-1}]$
<i>ss</i> Σ	0.350253(759)	-0.07202(728)	1.8841(1)	1.1470(251)	-54.2736(2388)
<i>pp</i> Σ	0.222384(1041)	0.38603(105)	-0.7931(699)	-1.1323(330)	54.7465(1.9753)
<i>dd</i> Σ	-0.135006(189)	0.10945(454)	-0.0835(296)	0.7342(33)	33.5579(1523)
<i>ff</i> Σ	-0.110015(844)	0.09303(1050)		0.5081(364)	-29.3589(2.2287)
<i>sp</i> Σ	0.155259(86)	0.02172(172)	-0.1981(225)	-0.5787(99)	
<i>pd</i> Σ	0.040476(1409)		-0.9768(714)	0.1780(441)	
<i>Df</i> Σ	-0.058289(714)		0.1169(618)	0.2016(89)	6.1484(2.4490)
<i>sd</i> Σ	-0.036860(1889)	-0.10847(190)	-3.2394(1)		3.7243(955)
<i>pf</i> Σ		0.11205(590)	-0.1381(1144)		
<i>sf</i> Σ	-0.046563(3111)	-0.07956(381)			
<i>pp</i> Π	-0.175842(572)	0.33476(162)	3.4038(151)	-0.6293(108)	6.1104(7858)
<i>dd</i> Π	-0.142924(444)	0.35589(264)	-2.9753(137)	0.5026(125)	-4.1589(4349)
<i>ff</i> Π	-0.039994(363)	0.05388(574)	-0.3467(212)		11.1237(1)
<i>pd</i> Π	0.171757(192)	-0.13954(166)	0.0911(169)	0.4246(88)	-62.8917(6833)
<i>df</i> Π	-0.014777(571)				7.6894(1134)
<i>pf</i> Π	0.040180(726)	0.03197(239)	-0.9735(328)		
<i>dd</i> Δ	-0.133587(292)	0.26062(97)	-0.0468(37)		
<i>ff</i> Δ	0.023472(290)	0.08906(191)			
<i>df</i> Δ	-0.031733(648)	-0.03388(119)			
<i>ff</i> Φ	0.095868(78)	0.22796(187)			

all of the $\partial\bar{\mu}_{\ell\ell'}^{(\Lambda)}/\partial R$ derivatives, nearly all of the $\partial\bar{\mu}_{\ell\ell'}^{(\Lambda)}/\partial\varepsilon$ derivatives for Σ and Π symmetry, and second derivatives ($\partial^2\bar{\mu}_{\ell\ell'}^{(\Lambda)}/\partial R^2$, $\partial^2\bar{\mu}_{\ell\ell'}^{(\Lambda)}/\partial\varepsilon^2$, and $\partial^2\bar{\mu}_{\ell\ell'}^{(\Lambda)}/\partial\varepsilon\partial R$) of the diagonal (*ss*, *pp*, *dd*, and *ff*) and many off-diagonal (*sp*, *pd*, *df*) quantum defects for Σ and Π symmetries. Some parameters could not be reliably determined (their values are not reported in Table I), and their values have been fixed at zero. Some of these parameters are very small and some are simply under-sampled by our input data. For example, a small number of $\partial\bar{\mu}_{\ell\ell'}^{(\Lambda)}/\partial R$ matrix elements, the values of which

are known from previous work³⁰ to be quite small, could not be determined here and were held fixed at zero. The $\bar{\mu}_{\text{ff}}^{(\Sigma)}$ defect, which has a strong quadratic energy dependence, appears to have no linear dependence on energy over our fitted range, and $\partial\bar{\mu}_{\text{ff}}^{(\Sigma)}/\partial\varepsilon$ was therefore also held fixed at zero. Many derivatives of $\bar{\mu}$ matrix elements of Δ and Φ symmetry are under-sampled: for example, sensitivity to the energy dependence of the quantum defects derives entirely from the coexistence of levels across a wide range of n^* in the same data set, and while all four symmetries

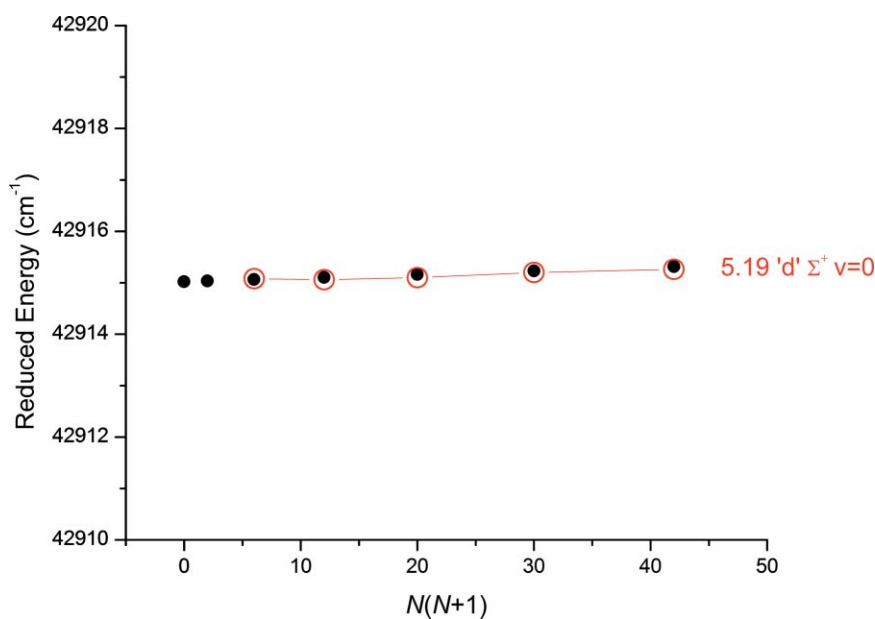


FIG. 1. Comparison of selected observed and calculated energy levels near $n^* = 5.0$, where vibronic states tend to be well-separated. For visual clarity, the reduced energy $E - B^+N(N + 1)$ is plotted against $N(N + 1)$ for each energy level. Filled circles indicate calculated energy levels and connected open circles indicate observed energy levels. Many levels with $n^* < 6.0$ are fitted to within 1 cm^{-1} , and most to within 5 cm^{-1} .

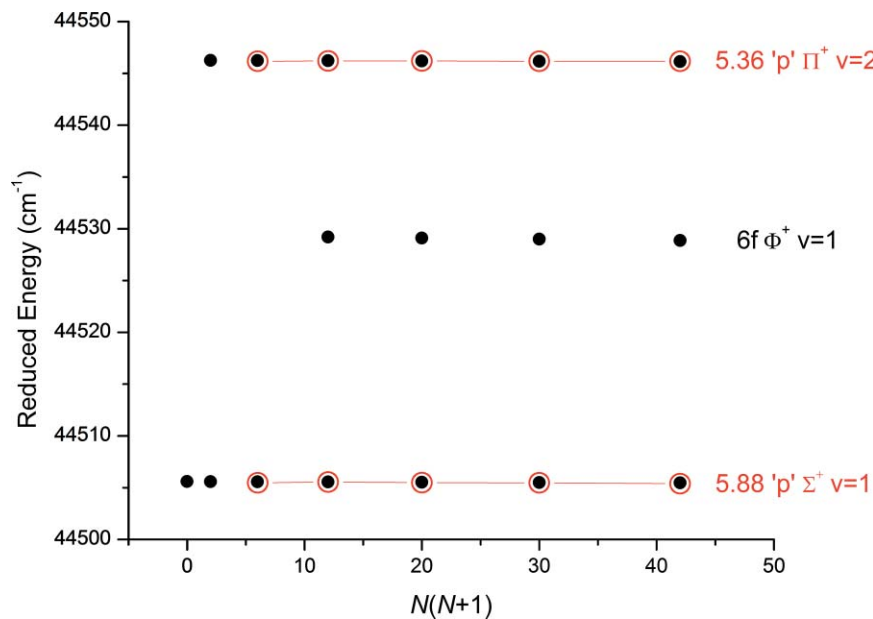


FIG. 2. Comparison of selected observed and calculated energy levels for vibrationally excited levels with low n^* . For visual clarity, the reduced energy $E - B^+N(N + 1)$ is plotted against $N(N + 1)$ for each energy level. Many levels with $n^* < 6.0$ are fitted to within 1 cm^{-1} , and most to within 5 cm^{-1} .

are represented at high n^* , most of the low n^* states included in the fit are of Σ and Π symmetry. (The lone core-penetrating Rydberg series of Δ symmetry, the 0.14 “d” Δ series,⁴³ is well-represented across the entire range and is responsible for our ability to determine the $\partial\bar{\mu}_{dd}^{(\Delta)}/\partial\varepsilon$ derivative.)

The magnitudes of all of the fit parameters appear reasonable. Thresholds for measurability of a fit parameter may be estimated based on a requirement that any parameter must cause a change in quantum defect of 0.02 over the range of ε ($\sim 5000\text{ cm}^{-1}$) and R ($1.87 \pm 0.13\text{ \AA}$, or 3.54

$\pm 0.24\text{ a}_0$) sampled in our fit in order to be *measurable*. We crudely estimate that the $\partial\bar{\mu}_{\ell\ell}^{(\Lambda)}/\partial R$, $\partial^2\bar{\mu}_{\ell\ell}^{(\Lambda)}/\partial R^2$, $\partial\bar{\mu}_{\ell\ell}^{(\Lambda)}/\partial\varepsilon$, $\partial^2\bar{\mu}_{\ell\ell}^{(\Lambda)}/\partial\varepsilon^2$, and $\partial^2\bar{\mu}_{\ell\ell}^{(\Lambda)}/\partial\varepsilon\partial R$ derivatives must have values of at least 0.04 a_0^{-1} , 0.08 a_0^{-2} , 0.50 Ry^{-1} , 12.50 Ry^{-2} , and $1.00\text{ a}_0^{-1}\text{ Ry}^{-1}$, respectively, to be reliably determined. To cause a *large change* in quantum defect of 0.2 over this range of ε and R , the parameters must have magnitudes ten times these values. The fitted derivatives fall in the ranges $0.0217\text{ a}_0^{-1} \leq |\partial\bar{\mu}_{\ell\ell}^{(\Lambda)}/\partial R| \leq 0.3860\text{ a}_0^{-1}$, $0.178\text{ a}_0^{-2} \leq |\partial^2\bar{\mu}_{\ell\ell}^{(\Lambda)}/\partial R^2| \leq 1.147\text{ a}_0^{-2}$, $0.047\text{ Ry}^{-1} \leq |\partial\bar{\mu}_{\ell\ell}^{(\Lambda)}/\partial\varepsilon| \leq 3.404\text{ Ry}^{-1}$, $4.16\text{ Ry}^{-2} \leq |\partial^2\bar{\mu}_{\ell\ell}^{(\Lambda)}/\partial\varepsilon^2| \leq 62.89\text{ Ry}^{-2}$,

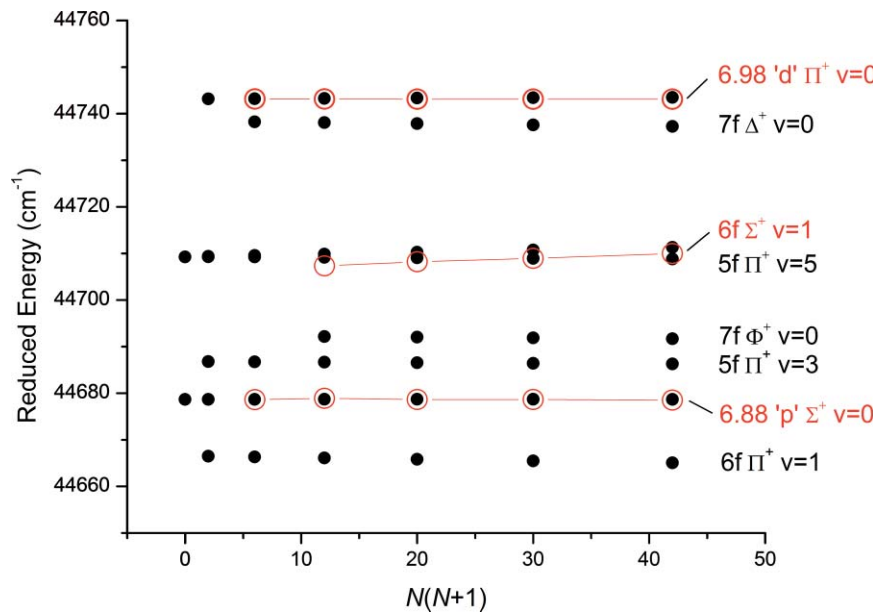


FIG. 3. Comparison of selected observed and calculated energy levels in the vicinity of $n^* = 7.0$. For visual clarity, the reduced energy $E - B^+N(N + 1)$ is plotted against $N(N + 1)$ for each energy level. Vibronic states at this energy are interleaved. Here, the classical period of electronic motion [proportional to $(n^*)^3$] is approximately equal to the classical period of vibrational motion. Vibronic perturbations are frequent.

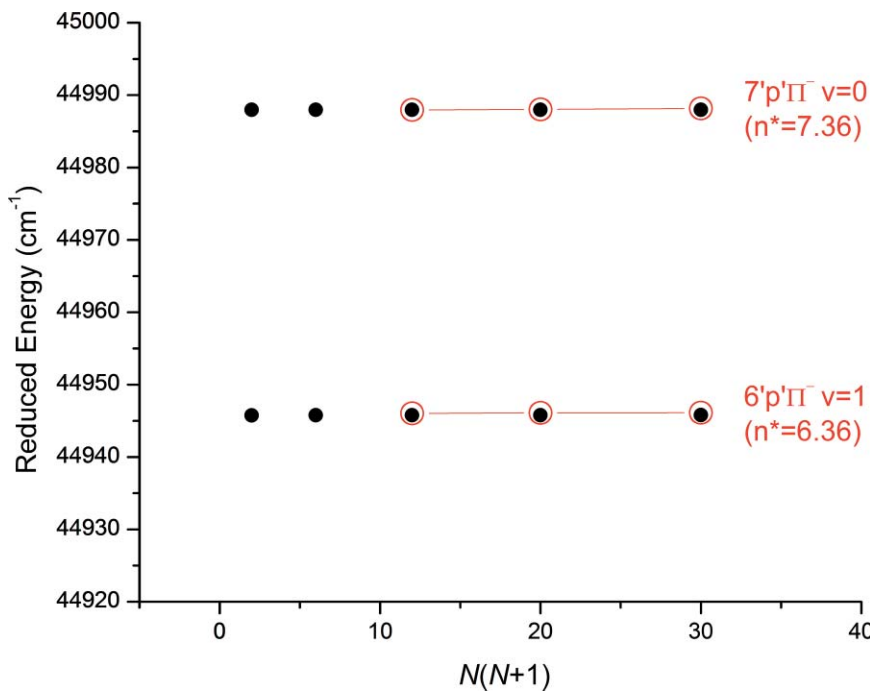


FIG. 4. Example of a strong vibronic (homogeneous) perturbation. In the absence of the perturbation, the 7.36 “ p' Π $v = 0$ and 6.36 “ p' Π $v = 1$ levels are nearly degenerate. The perturbation causes a $\sim 45 \text{ cm}^{-1}$ splitting of the levels and complete mixing of the two zero-order wavefunctions.

and $3.72 \text{ Ry}^{-1} a_0^{-1} \leq |\partial^2 \tilde{\mu}_{\ell\ell'}^{(\Lambda)} / \partial \varepsilon \partial R| \leq 11.12 \text{ Ry}^{-1} a_0^{-1}$. Thus, the smallest parameters determined in our fit have magnitudes which lie close to our crude sensitivity threshold estimates, and the largest parameters are capable of effecting changes of $\sim 0.1\text{--}0.2$ in the quantum defects over the range of ε and R sampled in our input data.

The quality of the fit is illustrated in Figs. 1–7, which show calculated and observed energy levels in seven portions of the fitted range. These seven portions are selected to illustrate varying degrees of spectroscopic complexity and

exhibit various dynamical features. In the figures, connected red circles represent observed energy levels and black dots represent energy levels calculated using the final values of the fit parameters shown in Table I. For visual clarity, for each vibronic level, we plot the “reduced energy” $E - B^+ N(N + 1)$ against $N(N + 1)$ (where B^+ is the rotational constant of the ion core) which tends to vertically magnify the rotational fine structure by removing the largest contribution to the total rotational energy. Rotational levels of vibronic states which conform to Hund’s case (b) coupling (for which N is the

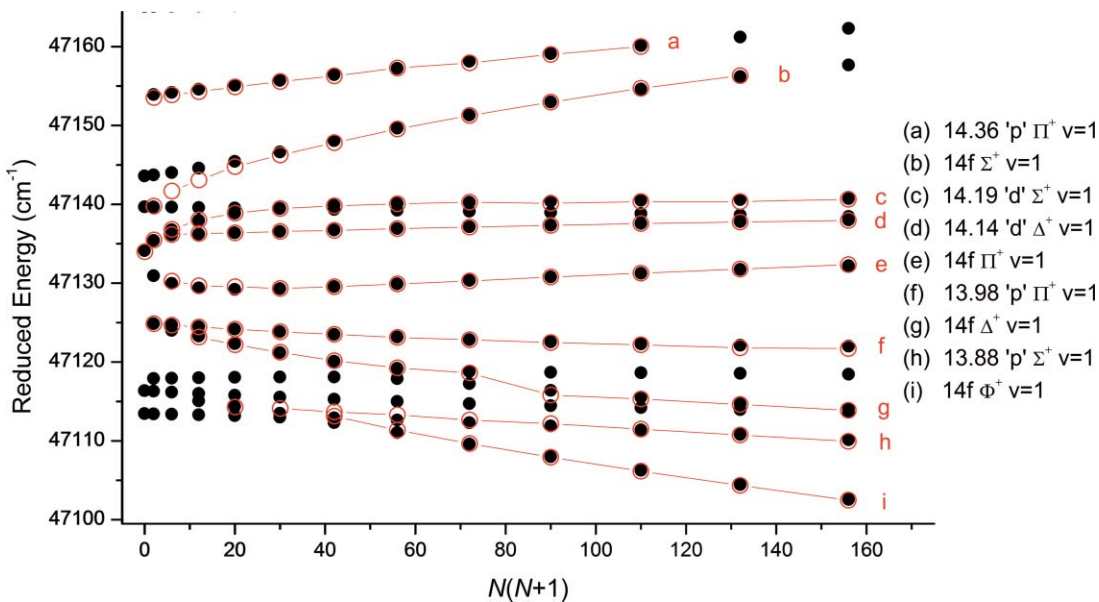


FIG. 5. Comparison of selected observed and calculated energy levels in the vicinity of $n^* = 14.0$. At this energy, the electronic energy level spacing is much smaller than the vibrational spacing, but still larger than the rotational spacing of the ion-core energy levels. Vibronic perturbations are uncommon, but rotational (inhomogeneous) perturbations become increasingly frequent.

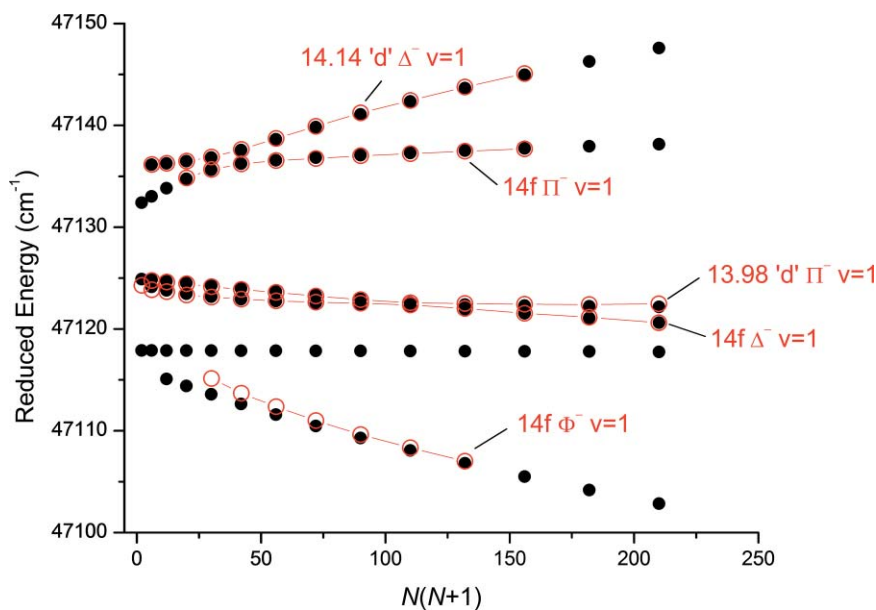


FIG. 6. Quality of fit in the $14f$ complex. A rotational perturbation between the $14f\ \Pi^-$ and $14.14\ "d"\ \Delta^-$ states gives rise to the avoided crossing at the top of the figure.

pattern-forming rotational quantum number) tend to lie along a horizontal line. This behavior is typical of core-penetrating Rydberg states with $n^* < 10$. Rotational levels of states which conform to Hund's case (d) coupling (for which the pattern-forming quantum number is N^+), or are intermediate between cases (b) and (d), will typically lie along a sloped line with some curvature, especially at low N . This behavior is typically exhibited by core-penetrating states with $n^* > 10$, and by core-nonpenetrating states at any energy.

The quality of the fit is uniformly excellent throughout the entire fitted range. At low energy ($n^* = 5 - 7$; Figs. 1–3),

where the fit quality is most sensitive to small variations in the fitted parameters, most levels tend to fit within 1 cm^{-1} and almost all fit to within 5 cm^{-1} . At higher energies ($n^* \approx 7$ and above; Figs. 4–7) the levels typically fit to within a few tenths of a cm^{-1} . The standard deviation of the residuals, including all observed levels (172 vibronic levels of 131 separate electronic states; 1017 individual rotational levels in all) is 1.57 cm^{-1} , but the bulk of the large residuals are concentrated in a small number of low-lying states. If we exclude the ten most poorly fit vibronic levels ($5.14\ "d"\ \Delta^+\ v = 0$, average residuals -4.97 cm^{-1} ; $5.55\ "s"\ \Sigma^+\ v = 0$, $+7.89\text{ cm}^{-1}$, $5f\ \Sigma^+$

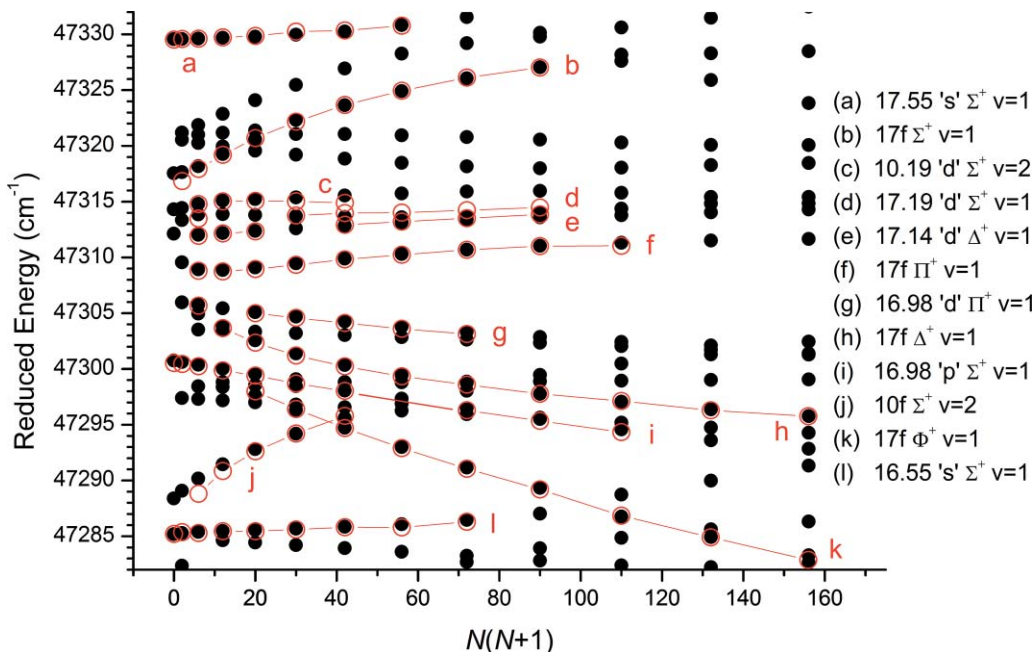


FIG. 7. Quality of fit in the $n^* = 16.5 - 17.5$ region. Above $n^* \sim 16$, rotational interactions are ubiquitous and quite strong, causing the disappearance of regular patterns which is evident here.

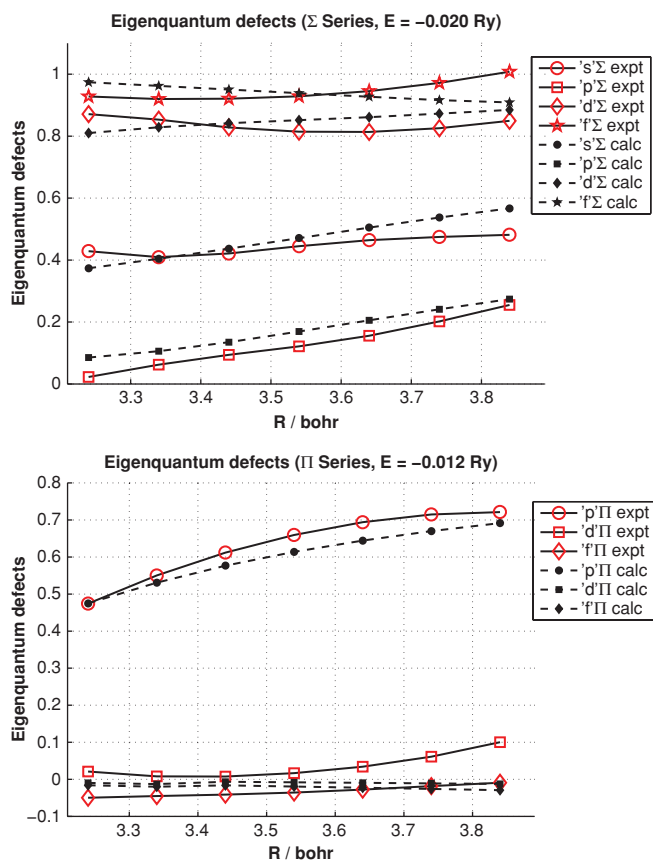


FIG. 8. R -dependence of MQDT-fitted and R-matrix calculated eigenquantum defects for (a) Σ and (b) Π series with $E = -0.020$ Ry ($n^* \approx 7.0$) and $E = -0.012$ Ry ($n^* \approx 9.0$), respectively. $R = 3.54 a_0$ is the equilibrium internuclear separation of the ion core.

$v = 0, -9.13 \text{ cm}^{-1}; 5.19 \text{ "d" } \Sigma^+ v = 2, -12.96 \text{ cm}^{-1}; 4.98 \text{ "d" } \Pi^+ v = 3, -3.15 \text{ cm}^{-1}; 5.98 \text{ "d" } \Pi^+ v = 1, -4.64 \text{ cm}^{-1}; 6f \Sigma^+ v = 1, -1.95 \text{ cm}^{-1}; 5.98 \text{ "d" } \Pi^- v = 0, -4.79 \text{ cm}^{-1}; 5.98 \text{ "d" } \Pi^- v = 1, -4.64 \text{ cm}^{-1}$; 37 rovibronic levels in all), which account for only 3.6% of the input data, the standard deviation of the fit decreases by 64% to 0.57 cm^{-1} .

Since the residuals arise from systematic model-based errors (as we discuss below) and clearly do not follow a normal distribution, a better statistical measure of the overall fit quality is therefore the *mean absolute error*, or the average of the absolute values of the residuals. The mean absolute error is 0.53 cm^{-1} with all observed levels included, but if we omit the ten most poorly fit vibronic levels listed above, the mean absolute error decreases to 0.27 cm^{-1} . As the mean absolute error indicates, the majority of observed levels do indeed fit to within a few tenths of one cm^{-1} . (A list of all observed levels, including fit residuals, can be found in the online supplementary material.³²)

Some systematic discrepancies do exist between the observed and fitted levels. The most notable disagreements involve the ten low-lying vibronic levels mentioned above, which have residuals of approximately $2\text{--}13 \text{ cm}^{-1}$. These are among the energetically lowest levels ($5.0 \leq n^* \leq 6.0$) included in the fit, and our inability to fit them perfectly implies that, at least for some of the quantum defects, our allowance of quadratic dependence on ϵ and/or R is not quite

adequate and that higher derivatives may be necessary to properly capture their dependences on ϵ and/or R . At the same time, this is clearly *not* the case for *all* quantum defects, as the great majority of rovibronic levels in the $5.0 \leq n^* \leq 6.0$ range fit quite well. In fact, if we omit the rest of the levels with $n^* < 6.0$ (30 vibronic levels, 228 rovibronic levels total, accounting for 22.4% of the input data set) from the calculation, the standard deviation and mean absolute error both *increase* slightly, to 0.59 cm^{-1} and 0.28 cm^{-1} , respectively.

The only other systematic discrepancies involve the nf Rydberg states: the energetically lowest $nf \Sigma^+$ states ($5f \Sigma^+$, $6f \Sigma^+$) are systematically predicted to be too high in energy, as are the lowest rotational levels of the energetically highest $nf \Sigma^+$ states. This discrepancy is likely due to the omission of g ($\ell = 4$) channels from the fit model. From previous work,³¹ it is evident that the nf states possess significant ng character, indicating that g channels do play a significant role in the dynamics. This possibility was not allowed here, since it would approximately double the number of adjustable parameters ($35 \bar{\mu}_{\ell\ell'}^{(A)}(R, \epsilon)$ functions for s, p, d, f , and g , vs $20 \bar{\mu}_{\ell\ell'}^{(A)}(R, \epsilon)$ functions for s, p, d , and f) and could impart excessive flexibility to the fit. Overall, the discrepancies between the observed and fitted levels are minimal and tend to be localized and rather small—at most a few cm^{-1} , even at the lowest energies.

The figures illustrate the wide range of dynamical timescales and phenomena captured by our fit model. Figure 1 shows a region ($n^* \approx 5$) in which vibronic states tend to be well separated: here, the classical frequency ($\propto n^{-3}$) of electronic motion is greater than the classical frequencies of vibration and rotation. Figure 2 shows the typical quality of the fit for vibrationally excited low- n^* levels. Figure 3 shows a region ($n^* \approx 7$) where the electronic motion has slowed and occurs on the timescale of vibration. Here, vibronic states are interleaved and $\Delta v \neq 0$ vibronic (electronic-vibrational) perturbations are quite common.

An example of a strong vibronic perturbation is shown in Fig. 4. Here, the $6.36 \text{ "p" } \Pi v = 1$ and $7.36 \text{ "p" } \Pi v = 0$ levels, which would be nearly degenerate in the absence of the perturbation, undergo a strong vibronic interaction, resulting in a $\sim 45 \text{ cm}^{-1}$ splitting of the levels and complete mixing of their wavefunctions.

Moving to higher energy, Fig. 5 shows a region ($n^* \approx 14$) where electronic motion is much slower than vibration and is approaching the timescale of rotation. In this region, $\Delta v \neq 0$ vibronic perturbations are uncommon, but $\Delta A \neq 0$ electronic-rotational perturbations become frequent.

An example of an electronic-rotational interaction is shown in Fig. 6, where the $14f \Pi^-$ and $14.14 \text{ "d" } \Delta^-$ states interact by ℓ -uncoupling ($-B\ell^\pm N^\mp$). At the very highest energies included in the fit, the frequency of electronic motion becomes nearly equal to the frequency of rotational motion of the ion-core (at high N), and electronic-rotational interactions become so frequent that regular patterns become difficult to identify. This vanishing of recognizable patterns is readily apparent in Fig. 7.

The fact that such a large and diverse collection of rovibronic levels are simultaneously fit, and the fact that *most* of

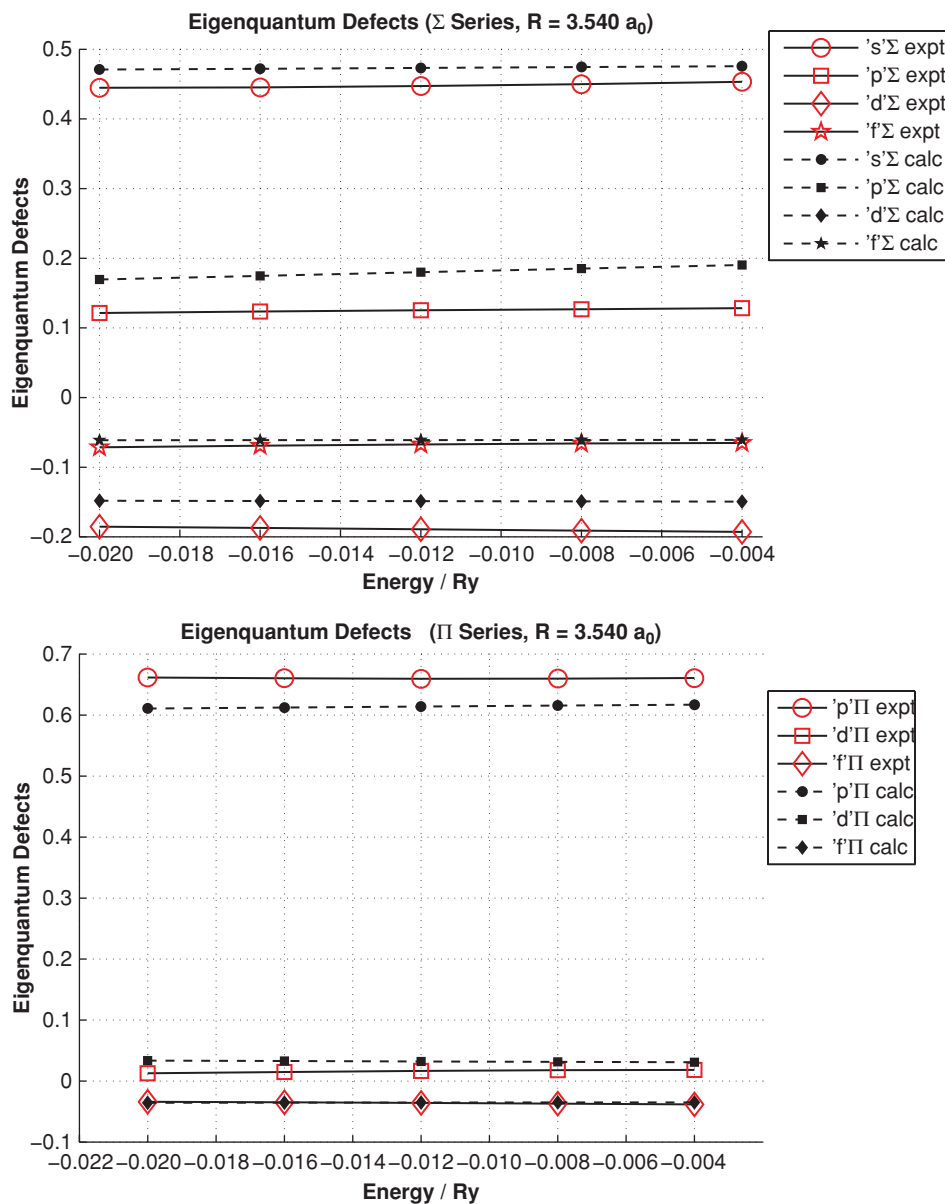


FIG. 9. Energy dependence of MQDT-fitted and R-matrix calculated Σ and Π series eigenquantum defects at the equilibrium internuclear separation, $R = 3.54 a_0$. Energy is in Rydberg units.

these levels are affected in some way by electronic-vibrational or electronic-rotational interactions, ensures the accuracy and completeness of our quantum defect model. With the exception of the effects of dissociation to neutral atoms, the quantum defect model we present here is *as complete as it possibly can be given the available theoretical methods and experimental observations to date*. Every observed energy level that can be fit has been included in the input data set. Unfortunately, the μ defects do not allow us to include the very lowest Rydberg states ($n^* < 5$) in the fit. As discussed in Refs. 13, 14, and 38, the μ and $\bar{\mu}$ defects allow the appearance of unphysical states with $n < \ell_{\max}$ (e.g., $3f$). This restricts our model to Rydberg states for which $n > \ell_{\max}$, and therefore we cannot consider Rydberg states with $n^* < 4.0$. Since these unphysical states with $n < \ell_{\max}$ also give rise to unphysical perturbations with real Rydberg states, we have further omitted all Rydberg states with $4.0 > n^* > 5.0$.

It is worth comparing our results here with the results of the previous CaF QDT fit,³⁰ which formed the starting point of the fit process, as discussed in Sec. IV B 1. Although our fit covers an energy range over an order of magnitude wider (5070 cm^{-1} here vs 401 cm^{-1} in Ref. 30), incorporates three times as many electronic states (131 electronic states here vs 43 in Ref. 30), extends across a much wider range of n^* ($5.0 < n^* < 20.0$ here, vs $12.5 < n^* < 14.5$ and $16.5 < n^* < 18.5$ in Ref. 30), includes many more rovibronic levels (1017 levels here vs 612 in Ref. 30), and allows for two times as many adjustable quantum defect parameters (74 here vs 38 in Ref. 30), the overall fit quality is largely identical to the previous results. As in Ref. 30, the vast majority of levels here fit to within $0.1\text{--}0.2 \text{ cm}^{-1}$, nearly to the accuracy of the experimental data. Since the present results cover a much wider range of n^* , the near-spectroscopic accuracy of our results (especially at low n^* , where small deviations in quantum

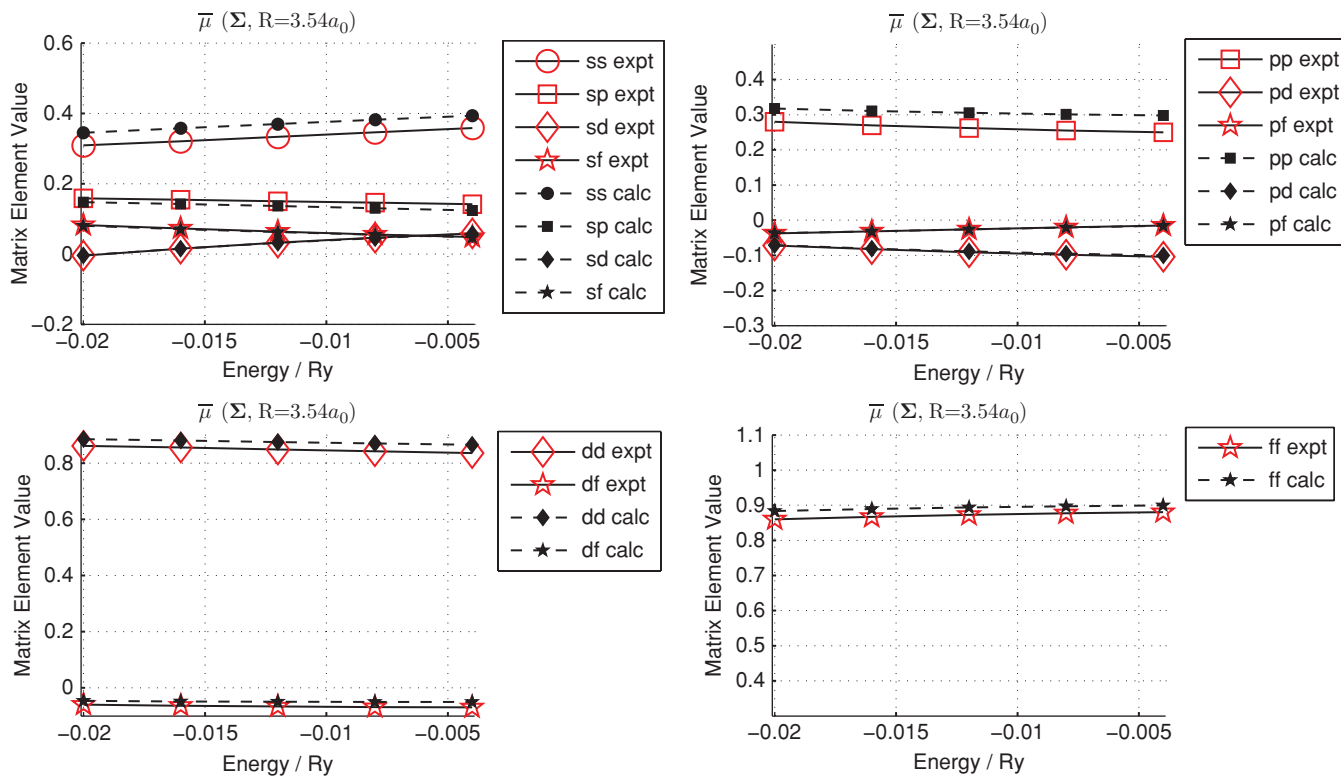


FIG. 10. Comparison of energy dependence of Σ series MQDT-fitted and R-matrix calculated $\bar{\mu}$ matrix elements, at the equilibrium internuclear separation, $R = 3.54 a_0$. Energy is in Rydberg units. The calculated $\bar{\mu}$ matrix elements have been adjusted as discussed in Appendix C to allow direct comparison with the fitted matrix elements.

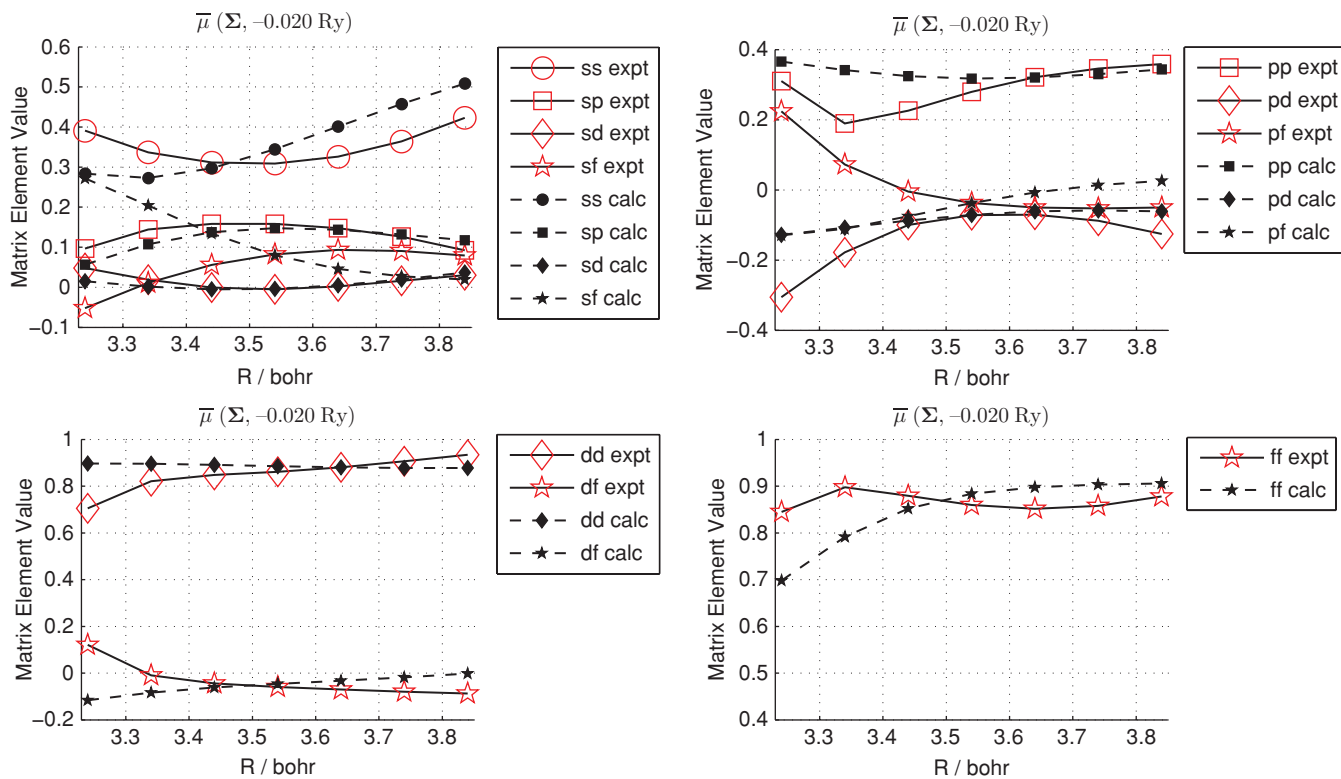


FIG. 11. R -dependence of MQDT-fitted and R-matrix calculated $\bar{\mu}$ matrix elements for Σ series, $E = -0.020$ Ry ($n^* \approx 7.0$). Trends with R show some differences from the experimental result away from the equilibrium R . (Also see Appendix C.) The calculated $\bar{\mu}$ matrix elements have been adjusted as discussed in Appendix C to allow direct comparison with the fitted matrix elements.

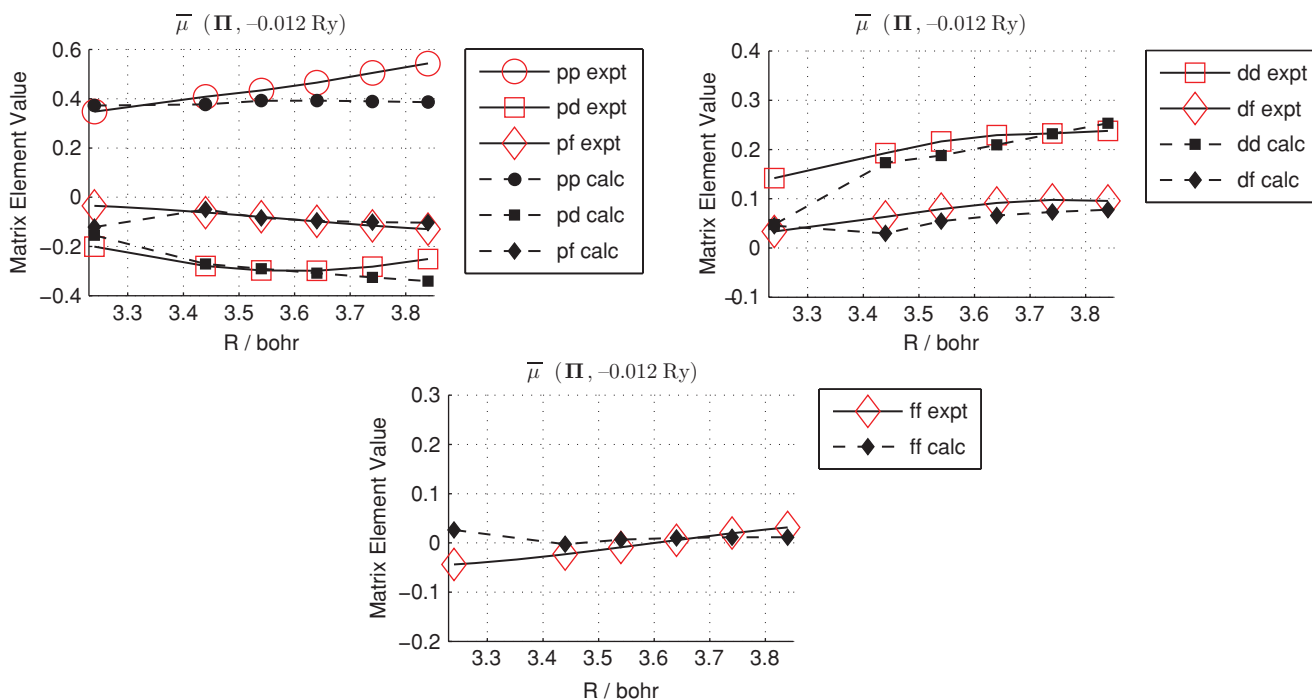


FIG. 12. Comparison of R -dependence of MQDT-fitted and **R**-matrix calculated $\bar{\mu}$ matrix elements for Π series, $E = -0.012$ Ry ($n^* \approx 7.0$). Trends with R show some differences from the experimental values away from R_e . (Also see Appendix C.) The calculated $\bar{\mu}$ matrix elements have been adjusted as discussed in Appendix C to allow direct comparison with the fitted matrix elements.

defect result in large deviations in energy) implies that the present fit determines the quantum defects to a very high level of accuracy. These results also sample a wider range of nonadiabatic interactions. The previous fit incorporated primarily $v = 1$ levels at high n^* affected by strong rotational-electronic (ℓ -uncoupling) interactions and occasional vibronic perturbations. As a result, the data were primarily sensitive to the ℓ - and Λ -dependences (and to some extent, the R -dependences) of the quantum defects and afford no sensitivity to their energy dependences. In contrast, the input data to our fit spans a much wider range of n^* and consequently samples numerous rotational-electronic interactions, numerous vibronic interactions, and a much wider range of collision energies. As a result, our data are highly sensitive not only to the ℓ - and Λ -dependence of the quantum defects, but are *also* highly sensitive to their energy- and R -dependences. Comparing our Table I to Table CI of Ref. 30, we note that our $\bar{\mu}_{\ell\ell}^{(\Lambda)}|_{R_e^+}$ matrix elements differ from the values reported in Ref. 30 typically in the second decimal place, implying differences of a few percent. Our $\partial\bar{\mu}_{\ell\ell}^{(\Lambda)}/\partial R$ matrix elements differ from those reported in Ref. 30 in the first decimal place, implying differences of tens of percent. These differences loosely indicate that the equilibrium matrix elements determined in Ref. 30 were well determined and likely indicates improvement in the R -dependence of the matrix elements as a result of the larger data set in the present work. However, we stress that it is not strictly appropriate to compare quantum defect derivatives from the two fits: in Ref. 30, the quantum defects were allowed only a linear dependence on internuclear distance. Here, we allow overall quadratic dependence on both internuclear distance and binding energy. A difference in a linear derivative between the two fits therefore does not necessarily

imply that the earlier result is less accurate: some of the difference could have been absorbed into the quadratic parameters, making a direct comparison of fitted parameters difficult.

D. R-matrix estimates of quantum defect matrix elements

To validate our fit model, we have performed **R**-matrix MQDT calculations across the experimentally accessed range of energy and internuclear separation using the CaF one-electron effective potential developed by Arif, Jungen, and Roche.^{26,45,46} The **R**-matrix approach⁴⁷ partitions the computational solution of the Schrödinger equation for the electron/ion system into a dynamically complex region near the ion-core and a long-range region of simpler dynamics. The **R**-matrix (wavefunction log derivative) expresses the wavefunction boundary conditions at the core boundary, and the vanishing of the wavefunction at infinite separation from the ion-core leads to the quantization condition of Eq. (8). We employ the dipole-reduced **R**-matrix/Green function propagator approach described in Refs. 45 and 46. This method provides a short-range **R** matrix that varies smoothly with ϵ and R by applying a monopole-dipole reduction as described in Refs. 45 and 46 and summarized in Appendix B. The semiempirical analytic potential described by Arif *et al.*²⁶ and used here, treats the ion-core as two polarizable atomic ions, with corrections for reduction of polarizability when the Rydberg electron penetrates into the core and for calcium atom core-shielding due to penetration [$Z_l^{\text{eff}}(r)$] of the Rydberg electron inside the closed shell ion-core. Arif *et al.*²⁶ showed that results from this effective potential compare well with experimental data at the equilibrium internuclear separation, R_e^+ .

We have done a more extensive calculation of the $\mathbf{K}^{(el)}$ and $\bar{\mu}^{(\Lambda)}$ matrices, eigenquantum defects, and wavefunction eigenchannel decompositions across the experimentally sampled ranges of energy and internuclear separation. Our computational method is summarized in Appendix B, and Appendix C describes some adjustments that are made to the R-matrix results to allow a direct comparison with the MQDT fitted parameters. The results of these calculations compare quite favorably with the parameters determined from the fit.

Figure 8 compares R-matrix calculated and MQDT-fitted eigenquantum defects for Σ and Π series, as a function of internuclear separation (at representative energies), and Fig. 9 displays the eigenquantum defects as a function of energy at the equilibrium internuclear separation. The agreement in energy dependence at $R = R_e^+ = 3.54 \text{ a}_0$ is generally good. The agreement in the internuclear distance dependence is good near R_e^+ , but degrades at larger and smaller values of R . Figures 10–12 compare individual elements of the $\bar{\mu}$ matrices determined in the fit with those predicted by the calculations. Figure 10 compares individual matrix elements as a function of energy, and Figs. 11 and 12 compare matrix elements as a function of R . The matrix elements agree very well as a function of energy and agree more loosely as a function of R . The departures between the calculated and fitted matrix elements at small and large R are more likely due to the neglect of some R -dependent effects in the effective one-electron potential used in these calculations, rather than a systematic inadequacy of the fit. A. J. Stone⁴⁸ has discussed at length the limitations and inaccuracies of this type of potential representation for electronic structure calculations. In addition, our new all-electron coupled-cluster single double (triple) calculations show that the R dependences of the dipole, quadrupole, and octupole moments of the CaF^+ ion-core are overestimated by the current effective potential.^{49,50} Nevertheless, this level of agreement between theory (which cannot be expected to reach spectroscopic accuracy) and experiment is excellent and validates the correctness of our fit model.

V. CONCLUSIONS

We have completed a global fit of nearly the entire observed electronic spectrum of CaF. This was made possible through the use of a fit strategy that employs physical intuition along with a combinatorial computational approach. The global fit model constructed in this process parameterizes the electronic spectrum and nearly all underlying dynamical processes in terms of a small number of quantum defect pa-

rameters. Nearly all observed energy levels ($5 < n^* < 20$, $0 < v < 3$, $0 < \ell < 3$, $0 < N < 12$) fit to within a fraction of one cm^{-1} . Comparison with R-matrix calculations further confirms the validity of the fitted parameters. This global fit model for CaF elevates the Rydberg states of CaF to an extremely high level of spectroscopic characterization, comparable to what has been achieved only for H_2 and NO.

Although the fit model we have presented here provides a *numerical* description of the spectrum and dynamics of the Rydberg states of CaF, the model alone does not provide insight into the underlying physical *mechanisms* for the exchange of energy and angular momentum between the Rydberg electron and the ion-core. It should be possible, however, to use ligand field theory, or theories based on a ligand-field picture,^{24,26–28} to explain the variations of the quantum defect matrix elements with ℓ , R , and ε , and to deduce the physical meanings of the quantum defects that form the heart of this model. This will provide greater insight, reduce the number of independently adjustable fit parameters, and enable the design of more mechanistically based models to describe electron-nuclear energy exchange and dynamics.

APPENDIX A: THE μ AND $\bar{\mu}$ QUANTUM DEFECTS

1. μ Defects

In the μ defect formulation,⁵¹ the matrix elements of the electronic reaction matrix $\mathbf{K}^{(el)}(R, \varepsilon)$ are given by

$$K_{\ell\ell'}^{(el)}(R, \varepsilon) = \tan(\pi\mu_{\ell\ell'}^{(\Lambda)}(R, \varepsilon)). \quad (\text{A1})$$

Diagonalization of $\mathbf{K}^{(el)}(R, \varepsilon)$ gives the eigenquantum defect matrix $\mu_{\alpha}^{(\Lambda)}(R, \varepsilon)$,

$$\mathbf{V}^T \mathbf{K}^{(el)}(R, \varepsilon) \mathbf{V} = \tan(\pi\mu_{\alpha}^{(\Lambda)}(R, \varepsilon)), \quad (\text{A2})$$

or equivalently,

$$\mathbf{K}^{(el)}(R, \varepsilon) = \mathbf{V} \tan(\pi\mu_{\alpha}^{(\Lambda)}(R, \varepsilon)) \mathbf{V}^T. \quad (\text{A3})$$

Note that the tan functions in Eqs. (A1) – (A3) are evaluated element-by-element. The matrix $\mu_{\alpha}^{(\Lambda)}(R, \varepsilon)$ is diagonal, with elements $\mu_{\alpha}^{(\Lambda)}(R, \varepsilon)$. The unitary matrix \mathbf{V} (which is also a function of both R and ε) diagonalizes $\mathbf{K}^{(el)}(R, \varepsilon)$, and its columns give the orbital angular momentum decomposition of the eigenchannels. The full rovibronic reaction matrix \mathbf{K} is given by

$$\begin{aligned} K_{\ell v^+ N^+, \ell' v^{+\prime} N^{+\prime}}^{(\text{rv})} &= \sum_{\Lambda} \langle \Lambda | N^+ \rangle^{(N, \ell, p)} \left[\int \chi_{v^+}^{(N^+)}(R) \tan(\pi\mu_{\ell\ell'}^{(\Lambda)}(R, \bar{\varepsilon}_{N^+ v^+, N^{+\prime} v^{+\prime}})) \chi_{v^{+\prime}}^{(N^{+\prime})}(R) dR \right] \langle N^{+\prime} | \Lambda \rangle^{(N, \ell', p)}, \\ &= \sum_{\Lambda} \langle \Lambda | N^+ \rangle^{(N, \ell, p)} \left[\int \chi_{v^+}^{(N^+)}(R) K_{\ell\ell'}^{(el)}(R, \bar{\varepsilon}_{N^+ v^+, N^{+\prime} v^{+\prime}}) \chi_{v^{+\prime}}^{(N^{+\prime})}(R) dR \right] \langle N^{+\prime} | \Lambda \rangle^{(N, \ell', p)}. \end{aligned} \quad (\text{A4})$$

The electronic reaction matrix elements $K_{\ell\ell'}^{(\text{el})}(R, \varepsilon) = \tan(\pi\mu_{\ell\ell'}^{(\Lambda)}(R, \varepsilon))$ in the integrand of Eq. (A4) are singular at the point $\mu_{\ell,\ell'}^{(\Lambda)}(R, \varepsilon) = 1/2$.

2. $\bar{\mu}$ Defects

A smoother parameterization may be devised³⁸ by simply removing the tangent function of Eq. (A3), defining the matrix

$\bar{\mu}^{(\Lambda)}(R, \varepsilon)$ (matrix elements $\bar{\mu}_{\ell\ell'}^{(\Lambda)}(R, \varepsilon)$):

$$\bar{\mu}^{(\Lambda)}(R, \varepsilon) \equiv \mathbf{V}\mu_{\alpha}^{(\Lambda)}(R, \varepsilon)\mathbf{V}^T, \quad (\text{A5})$$

where \mathbf{V} is the matrix that diagonalizes $\mathbf{K}^{(\text{el})}(R, \varepsilon)$, and $\mu_{\alpha}^{(\Lambda)}(R, \varepsilon)$ is the matrix of eigenquantum defects. The potentially singular matrix elements $K_{\ell\ell'}^{(\Lambda)}(R, \varepsilon) = \tan(\pi\mu_{\ell\ell'}^{(\Lambda)}(R, \varepsilon))$ in the integrand of Eq. (A4) are replaced with smoothly varying matrix elements, $\bar{\mu}_{\ell\ell'}^{(\Lambda)}(R, \varepsilon)$:

$$M_{\ell v^+ N^+, \ell' v^+ N'^+} = \sum_{\Lambda} \langle \Lambda | N^+ \rangle^{(N, \ell, p)} \left[\int \chi_{v^+}^{(N^+)}(R) \bar{\mu}_{\ell\ell'}^{(\Lambda)}(R, \bar{\varepsilon}_{N^+ v^+, N'^+ v'^+}) \chi_{v'^+}^{(N'^+)}(R) dR \right] \langle N'^+ | \Lambda \rangle^{(N, \ell, p)}, \quad (\text{A6})$$

and $\bar{\mu}^{(\Lambda)}(R, \varepsilon)$ plays the same role as the matrix $\mathbf{K}^{(\text{el})}(R, \varepsilon)$ in Eq. (A4). To calculate the energy levels, we then recover the *original* rovibronic reaction matrix $\mathbf{K}^{(\text{rv})}$ of Eq. (A4) using the relationship

$$\mathbf{K}^{(\text{rv})} = \mathbf{U} \tan(\pi \mathbf{U}^T \mathbf{M} \mathbf{U}) \mathbf{U}^T. \quad (\text{A7})$$

Here, \mathbf{U} is the matrix that diagonalizes the matrix \mathbf{M} of Eq. (A6).

The smoothness of $\bar{\mu}^{(\Lambda)}(R, \varepsilon)$, which is responsible for the success of this formulation, is a result of the fact that $\bar{\mu}^{(\Lambda)}(R, \varepsilon)$ is explicitly defined in terms of the eigenquantum defects, $\mu_{\alpha}^{(\Lambda)}(R, \varepsilon)$, and the matrix \mathbf{V} . The eigenquantum defects $\mu_{\alpha}^{(\Lambda)}(R, \varepsilon)$ (which give the electronic energy levels of the nonrotating molecule) and the matrix \mathbf{V} (which gives the orbital angular momentum decomposition of the electronic reaction matrix, $\mathbf{K}^{(\text{el})}(R, \varepsilon)$, i.e., the $s \sim p \sim d \sim f$ mixed characters of the electronic wavefunctions), must themselves be smooth, since they can be derived, respectively, from the Born–Oppenheimer potential energy curves and Born–Oppenheimer molecular wavefunctions.

1. Transformation between μ and $\bar{\mu}$ defects

To derive the transformation between the two formulations, we rewrite Eq. (A3) as

$$\mu_{\alpha}^{(\Lambda)}(R, \varepsilon) = \frac{1}{\pi} \arctan(\mathbf{V}^T \mathbf{K}^{(\Lambda)}(R, \varepsilon) \mathbf{V}), \quad (\text{A8})$$

and, since $\bar{\mu}^{(\Lambda)}(R, \varepsilon) \equiv \mathbf{V}\mu_{\alpha}^{(\Lambda)}(R, \varepsilon)\mathbf{V}^T$,

$$\bar{\mu}^{(\Lambda)}(R, \varepsilon) = \mathbf{V} \left[\frac{1}{\pi} \arctan(\mathbf{V}^T \mathbf{K}^{(\Lambda)}(R, \varepsilon) \mathbf{V}) \right] \mathbf{V}^T. \quad (\text{A9})$$

Rearranging Eq. (A9) (compare Eq. (A7)),

$$\mathbf{K}^{(\Lambda)}(R, \varepsilon) = \mathbf{V} \tan(\pi \mathbf{V}^T \bar{\mu}^{(\Lambda)}(R, \varepsilon) \mathbf{V}) \mathbf{V}^T. \quad (\text{A10})$$

Matrix elements of $\mu^{(\Lambda)}(R, \varepsilon)$ are then recovered from Eq. (A10) using the relationship

$$\mu_{\ell\ell'}^{(\Lambda)}(R, \varepsilon) = \frac{1}{\pi} \arctan \left(K_{\ell\ell'}^{(\Lambda)}(R, \varepsilon) \right). \quad (\text{A11})$$

APPENDIX B: SUMMARY OF R-MATRIX CALCULATION METHOD

The **R**-matrix calculation method used here is largely derived from the long history of **R**-matrix calculations, but includes some unique features that make possible our direct comparison to experimental data. Primary among them are the use of a dipole reduction of the Hamiltonian and the computation of the physical short-range reaction matrix in spherical coordinates centered at the Ca atom. The method is described in some detail in Refs. 26, 45, and 46. Our current calculation largely follows Refs. 26, 45, and 46, with some minor differences. This Appendix provides a schematic overview of our method.

1. Dipole reduction of Hamiltonian

The large dipole moment in the CaF^+ core influences wavefunctions and quantum defects through the mixing of Rydberg electron angular momentum states.^{28,52–55} By prediagonalizing the monopole and dipole parts of the potential, we are able to shrink the reaction zone and reduce the distance at which the long-range boundary condition is imposed. The dipole value is determined by a Gauss’ law integral of the potential. The solution is expressed in the prediagonalized system in terms of Coulomb functions for fractional or imaginary angular momentum described by Dubau.⁵⁶ However, those functions are linearly related to standard integer- ℓ Coulomb functions.

2. Variational solution

The dipole-reduced problem is solved using the Kohn variational approach to the **R**-matrix method.^{47,57} In the

R-matrix method the log-derivatives of the wavefunction are computed on a boundary surface. The Kohn variational method converts the solution for the log-derivative to a matrix equation involving integrals of the Hamiltonian with basis functions defined within the bounded region. Computing these Hamiltonian integrals is time consuming and requires integration over the Ca core, including the nucleus at which the potential diverges. To ensure the accuracy of these integrations, we use two concentric spherical boundary surfaces centered at Ca: (i) an atomic zone around the Ca atom or Ca^{++} ion, and (ii) a molecular zone outside Ca but containing CaF. Only spherically symmetric terms in the potential are used in the atomic zone. Finally, a Green function propagator is used iteratively to find the electronic reaction matrix, $\mathbf{K}_{\text{calc}}^{(\text{el})(\Lambda)}$, which satisfies both the log-derivative condition at the molecular zone boundary and the long-range vanishing of the wavefunction. This procedure is more fully described in Sec. 2 C of Ref. 45.

3. Computation of $\bar{\mu}_{\text{calc}}^{(\Lambda)}$ and quantum defects

A set of calculated quantum defects, $\bar{\mu}_{\text{calc}}^{(\Lambda)}$, can be generated from the calculated electronic reaction matrix, $\mathbf{K}_{\text{calc}}^{(\text{el})(\Lambda)}$, and can be directly compared to the fitted parameters, $\bar{\mu}_{\text{fit}}^{(\Lambda)}$. The relationship between $\mathbf{K}^{(\text{el})}$ and $\bar{\mu}^{(\Lambda)}$ is described in Appendix A. The eigenquantum defects μ_α , which have unit periodicity, are calculated as an intermediate step in the transformation and are adjusted into the same unit range as the experimental eigenquantum defects prior to the final step of the transformation.

4. Adjustment of calculated values for comparison with fitted values

a. State selection

The angular momentum basis used in the calculation includes $0 \leq \ell \leq 6$, whereas the fit only allowed for $0 \leq \ell \leq 3$. Electronic eigenchannels predicted by the calculation were selected for comparison with the fitted eigenchannels based on channel mixing coefficients and relative signs.

b. Basis rotation

A rotation, or a difference in basis between $\bar{\mu}_{\text{calc}}^{(\Lambda)}$ and $\bar{\mu}_{\text{fit}}^{(\Lambda)}$ is observed. This basis rotation can be minimized by an orthogonal transformation, which we choose to be independent of internuclear separation R . The relative rotation between the fitted and calculated matrices is seen to be greater for Π than for Σ states. Correcting for this rotation improves the agreement between $\bar{\mu}_{\text{fit}}^{(\Lambda)}$ and $\bar{\mu}_{\text{calc}}^{(\Lambda)}$ without affecting the eigenquantum defects. The rotation may be an edge effect arising from exclusion of high orbital angular momentum channels (g, h, i) from the fit model.

The parameters used in the calculation include the radius of the Ca atomic zone, $r_a = 0.8 \text{ a}_0$, the radius of the molecular zone, $r_o = 7 \text{ a}_0$, and the radius of the dipole-reduced long-range zone, $r_c = 15 \text{ a}_0$. The value of r_c is significantly smaller than the radius used without dipole reduction. The angular momentum basis set size was limited to $\ell \leq 6$. This basis set size was required at the lowest calculated energy, $E = -0.02 \text{ Ry}$, by the requirement that $\ell \leq n - 1$. Internuclear separation, R , was varied from 3.24 to 3.84 a_0 in steps of 0.1 a_0 , and the energy was varied from -0.020 to -0.004 Ry in steps of 0.004 Ry at each value of R . These values cover much of the experimental ranges of energy and the vibrational motion in R . In order to compare data for the states described by the fitted and calculated $\bar{\mu}$, it is necessary to correctly match states from the fitted group to the calculated group. We find that this matching can be accomplished based on the magnitudes and relative signs of the eigenchannel decompositions.

Because it uses a large angular momentum basis set, the calculation reveals additional detail about the mixing in of higher- ℓ basis states that are outside of the $s-p-d-f$ block included in the fit. This out-of-block mixing suggests an explanation for the enhanced electronic transition access to non-penetrating states that has been observed experimentally.³¹ Figure B1 shows that the state of nominal f character contains contributions of g (10%) and h (2–4%) characters that vary as a function of R . Similarly, the calculated g and h states (not shown) show approximately 9% and 2% f character, resulting in the observable intensities of transitions from lower, nominally core-penetrating states into these highly nonpenetrating Rydberg states.

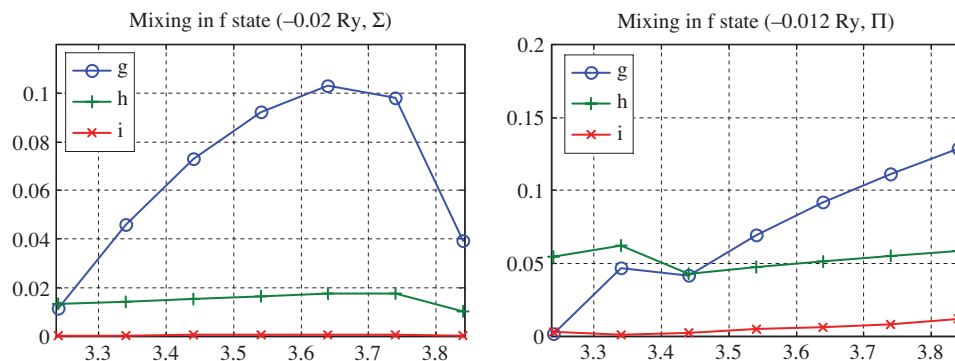


FIG. B1. Calculated R -dependence of higher- ℓ mixing in Σ and Π states of dominant f character, at $E = -0.02 \text{ Ry}$. The calculation predicts mixing outside of the experimentally fitted s, p, d, f block dominantly to g character, but also to h . These mixings enhance experimental access to non-penetrating states, as reported in Kay *et al.* (Ref. 31).

TABLE CI. $\mathbf{U}_{\text{CF}}(R = 3.54 \text{a}_0)$ matrix for Σ symmetry.

Fit \ Calc	<i>s</i>	<i>p</i>	<i>d</i>	<i>f</i>	<i>g</i>	<i>h</i>	<i>i</i>
<i>s</i>	-0.9796	-0.0946	0.1766	-0.0017	-0.0084	0.0115	-0.0020
<i>p</i>	-0.1028	0.9913	-0.0407	0.0674	-0.0236	0.0089	-0.0016
<i>d</i>	0.0296	0.0827	0.2230	-0.9043	0.3340	-0.1137	0.0177
<i>f</i>	0.1698	0.0403	0.9567	0.2005	-0.0971	0.0677	-0.0117
<i>g</i>	-0.0054	-0.0008	0.0314	0.3690	0.8997	-0.2306	0.0110
<i>h</i>	0.0030	-0.0014	-0.0358	-0.0352	0.2605	0.9461	-0.1859
<i>i</i>	0.0000	0.0002	0.0005	0.0080	0.0320	0.1846	0.9823

APPENDIX C: BASIS ROTATION BETWEEN CALCULATED AND FITTED $\bar{\mu}$

Using the notation of Appendix A and Ref. 58, calculated and fitted $\bar{\mu}$ matrices can be diagonalized to determine the eigenquantum defects μ_α that approximate the true values. This can be expressed in terms of column eigenvectors as

$$\begin{aligned} \bar{\mu}_{\text{fit}} \mathbf{U}_{\text{fit}} &= \mathbf{U}_{\text{fit}} \mu_{\alpha, \text{fit}}, \\ \bar{\mu}_{\text{calc}} \mathbf{U}_{\text{calc}} &= \mathbf{U}_{\text{calc}} \mu_{\alpha, \text{calc}}, \\ \mu_{\alpha, \text{calc}} &= \mathbf{U}_{\text{calc}}^T \bar{\mu}_{\text{calc}} \mathbf{U}_{\text{calc}} \cong \mu_{\alpha, \text{TRUE}} \cong \mathbf{U}_{\text{fit}}^T \bar{\mu}_{\text{fit}} \mathbf{U}_{\text{fit}} = \mu_{\alpha, \text{fit}}. \end{aligned} \quad (\text{C1})$$

Our comparisons of fitted and calculated $\bar{\mu}$ matrices indicate the presence of an orthogonal transformation or rotation between the fitted and calculated basis sets that is small for Σ states and moderate for Π states. The agreement between fitted and calculated $\bar{\mu}$ is improved if we transform the calculated $\bar{\mu}$ to the same basis as the fitted $\bar{\mu}$. Because eigenvalues are unchanged by such a transformation, the comparison between fitted and calculated eigenquantum defects is unaffected.

An estimate of the basis rotation between the two systems is given by the relative rotation of eigenvectors, $\mathbf{U}_{\text{CF}} \equiv \mathbf{U}_{\text{calc}} \mathbf{U}_{\text{fit}}^T$, where \mathbf{U}_{fit} is increased to the size of \mathbf{U}_{calc} by adding ones on the diagonal as if *g*, *h*, and *i* orbital angular momentum waves were fully non-interacting. Using equation (C1), the fitted $\bar{\mu}$ can be calculated from the calculated eigenquantum defects, $\mu_{\alpha, \text{calc}}$, effectively transforming the calculated $\bar{\mu}$ to the fit basis:

$$\begin{aligned} \bar{\mu}_{\text{calc(fit)}} &\equiv \mathbf{U}_{\text{CF}}^T \bar{\mu}_{\text{calc}} \mathbf{U}_{\text{CF}} = (\mathbf{U}_{\text{fit}} \mathbf{U}_{\text{calc}}^T) \bar{\mu}_{\text{calc}} (\mathbf{U}_{\text{calc}} \mathbf{U}_{\text{fit}}^T) \\ &= \mathbf{U}_{\text{fit}} \mu_{\alpha, \text{calc}} \mathbf{U}_{\text{fit}}^T. \end{aligned} \quad (\text{C2})$$

By this transformation, the $\bar{\mu}_{\text{calc}}$ matrix is adapted for any difference in basis between the fit and the calculation.

TABLE CII. $\mathbf{U}_{\text{CF}}(R = 3.54 \text{a}_0)$ matrix for Π symmetry.

Fit \ Calc	<i>p</i>	<i>d</i>	<i>f</i>	<i>g</i>	<i>h</i>	<i>i</i>
<i>p</i>	0.9753	-0.2140	0.0082	0.0311	-0.0420	0.0106
<i>d</i>	0.1278	0.6030	-0.7535	0.2078	-0.0913	0.0272
<i>f</i>	0.1772	0.7597	0.5588	-0.1938	0.1943	-0.0625
<i>g</i>	-0.0286	0.0609	0.3239	0.9129	-0.2387	-0.0175
<i>h</i>	0.0124	-0.0971	-0.1154	0.2872	0.9287	-0.1795
<i>i</i>	-0.0010	0.0173	0.0411	0.0503	0.1810	0.9812

Two R -dependent effects are noticeable, (i) a difference in basis orientation at $R = 3.54 \text{ a}_0$ and (ii) a difference in the R -dependence of eigenchannel decompositions. If we choose to utilize the transformation computed for $R = 3.54 \text{ a}_0$ at all R , $\bar{\mu}_{\text{calc(fit)}}$ can be calculated either using $\mathbf{U}_{\text{CF}}(R = 3.54 \text{ a}_0)$ in $\mathbf{U}_{\text{CF}}^T \bar{\mu}_{\text{calc}} \mathbf{U}_{\text{CF}}$, or $\mathbf{U}_{\text{fit}}(R = 3.54 \text{ a}_0)$ in $\mathbf{U}_{\text{fit}} \mu_{\alpha, \text{calc}} \mathbf{U}_{\text{fit}}^T$. The use (at all R) of the transformation for $R = 3.54 \text{ a}_0$ maintains some level of independence between the compared matrix elements, both in value and in R derivatives.

We have chosen the first method, using $\mathbf{U}_{\text{CF}}(R = 3.54 \text{ a}_0)$, because it reveals the difference in R dependence of channel mixing coefficients between the current calculation and the fit, while the second method suppresses those differences. Other methods of reconciling the two basis sets can be defined, including the use of singular value decomposition to determine a single least-squares optimized transformation,⁵⁹ but in the absence of an interpretation for the transformation, we have selected this fixed- R approach.

Tables CI and CII show $\mathbf{U}_{\text{CF}}(R = 3.54 \text{ a}_0)$ for Σ and Π states. The rotation is nearly diagonal except for *d* and *f* states in both cases.

¹T. Baer and W. Hase, *Unimolecular Reaction Dynamics* (Oxford University Press, New York 1996); R. Schinke *Photodissociation Dynamics* (Cambridge University Press, Cambridge, England, 1993); A. Tramer, Ch. Jungen, and F. Lahmani, *Energy Dissipation in Molecular Systems* (Springer, Berlin, 2005).

²A beautiful example of dynamical complexity in a “simple” diatomic system can be found in the photophysics of NO; see H. Park and R. N. Zare, *Phys. Rev. Lett.* **6**, 1591 (1996); H. Park, I. Konen, and R. N. Zare, *ibid.* **4**, 3819 (2000); A. Fujii and N. Morita, *J. Chem. Phys.* **98**, 4581 (1993); A. Fujii and N. Morita, *Laser Chemistry* **13**, 259 (1994), S. T. Pratt, *J. Chem. Phys.* **108**, 7131 (1998), and references therein.

³H. Lefebvre-Brion and R. W. Field, *The Spectra and Dynamics of Diatomic Molecules* (Elsevier, San Diego, 2004).

⁴R. S. Mulliken, *J. Am. Chem. Soc.* **86**, 3183 (1964).

⁵P. Labastie, M. C. Bordas, B. Tribollet, and M. Broyer, *Phys. Rev. Lett.* **52**, 1681 (1984).

⁶M. Lombardi, P. Labastie, M. C. Bordas, and M. Broyer, *J. Chem. Phys.* **89**, 3479 (1988).

⁷H. J. Wörner, S. Mollet, Ch. Jungen, and F. Merkt, *Phys. Rev. A* **75**, 062511 (2007).

⁸J. J. Kay, S. N. Altunata, S. L. Coy, and R. W. Field, *Mol. Phys.* **105** (11–12), 1661–1673 (2007).

⁹D. Dill and Ch. Jungen, *J. Phys. Chem.* **84**, 2116 (1980).

¹⁰U. Fano, *Phys. Rev. A* **2**, 353 (1970).

¹¹Ch. Jungen and O. Atabek, *J. Chem. Phys.* **66**, 5584 (1977).

¹²M. J. Seaton, *Rep. Prog. Phys.* **46**, 167 (1983).

¹³C. H. Greene and Ch. Jungen, *Adv. At. Mol. Phys.* **21**, 51 (1985).

¹⁴Ch. Jungen, *Molecular Applications of Quantum Defect Theory* (Taylor & Francis, London, 1996).

- ¹⁵S. Ross, in *Half-Collision Resonance Phenomena in Molecules*, edited by M. Garcia-Sucre, G. Raseev, and S. C. Ross, (American Institute of Physics, New York, 1991).
- ¹⁶S. Ross and Ch. Jungen, *Phys. Rev. Lett.* **59**, 1297 (1987).
- ¹⁷A. Matzkin, Ch. Jungen, and S. C. Ross, *Phys. Rev. A* **62**, 062511 (2000).
- ¹⁸H. Gao, Ch. Jungen, and C. H. Greene, *Phys. Rev. A* **47**(6), 4877 (1993).
- ¹⁹Ch. Jungen, *Phys. Rev. Lett.* **53**, 2394 (1984).
- ²⁰Ch. Jungen and S. C. Ross, *Phys. Rev. A* **55**, R2503 (1997).
- ²¹J. E. Murphy, J. M. Berg, A. J. Merer, Nicole A. Harris, and R. W. Field, *Phys. Rev. Lett.* **65**, 1861 (1990).
- ²²J. M. Berg, J. E. Murphy, N. A. Harris, and R. W. Field, *Phys. Rev. A* **48**, 3012 (1993).
- ²³N. A. Harris and R. W. Field, *J. Chem. Phys.* **98**, 2642 (1993).
- ²⁴N. A. Harris and Ch. Jungen, *Phys. Rev. Lett.* **70**, 2549 (1993).
- ²⁵N. A. Harris, Ph.D. dissertation, Massachusetts Institute of Technology, 1995.
- ²⁶M. Arif, Ch. Jungen, and A. L. Roche, *J. Chem. Phys.* **106**, 4102 (1997).
- ²⁷S. Raouafi, G.-H. Jeung, and Ch. Jungen, *J. Chem. Phys.* **115**, 7450 (2001).
- ²⁸Ch. Jungen and A. L. Roche, *Can. J. Phys.* **79**, 287 (2001).
- ²⁹J. J. Kay, D. S. Byun, J. O. Clevenger, X. Jiang, V. S. Petrovic, R. Seiler, J. R. Barchi, A. J. Merer, and R. W. Field, *Can. J. Chem.* **82**, 791 (2004).
- ³⁰R. W. Field, C. M. Gittins, N. A. Harris, and Ch. Jungen, *J. Chem. Phys.* **122**, 184314 (2005).
- ³¹J. J. Kay, S. L. Coy, V. S. Petrović, Bryan M. Wong, and R. W. Field, *J. Chem. Phys.* **128**, 194301 (2008).
- ³²See supplementary material at <http://dx.doi.org/10.1063/1.3565967> for a list of all energy levels included in the fit.
- ³³S. Gerstenkorn and P. Luc, *Atlas du spectre d'absorption de la molécule Iode*, Editions du C.N.R.S (C.N.R.S. II, Orsay, France, 1978).
- ³⁴R. K. Nesbet, *Phys. Rev. A* **19**, 551 (1979).
- ³⁵Ch. Jungen and G. Raseev, *Phys. Rev. A* **57**, 2407 (1998).
- ³⁶Ch. Jungen and A. L. Roche, *J. Chem. Phys.* **110**, 10784 (1999).
- ³⁷S. Ross and Ch. Jungen, *Phys. Rev. A* **50**, 4618 (1994).
- ³⁸S. Ross and Ch. Jungen, *Phys. Rev. A* **49**, 4364 (1994).
- ³⁹K. P. Huber and G. Herzberg, *Molecular Spectra and Molecular Structure. IV: Constants of Diatomic Molecules* (Van Nostrand Reinhold, New York, 1979).
- ⁴⁰A. Giusti-Suzor and Ch. Jungen, *J. Chem. Phys.* **80**, 986 (1984).
- ⁴¹Ch. Jungen and S. C. Ross, *Phys. Rev. A* **55**, R2503 (1997).
- ⁴²A. Matzkin, Ch. Jungen, and S. C. Ross, *Phys. Rev. A* **62**, 062511 (2000).
- ⁴³The strongly ℓ -mixed core-penetrating Rydberg series of CaF are often referred to by their values of n^* modulo 1: 0.55 "s"Σ, 0.88 "p"Σ, 0.19 "d"Σ, 0.36 "p"Π, 0.98 "d"Π, and 0.14 "d"Δ. The core-nonpenetrating series tend to retain their pure- ℓ characters and are described using the traditional notation: fΣ, fΠ, fΔ, and fΦ.
- ⁴⁴A. F. Ruckstuhl, W. A. Stahel, and K. Dressler, *J. Mol. Spectrosc.* **160**, 434 (1993).
- ⁴⁵S. N. Altunata, S. L. Coy, and R. W. Field, *J. Chem. Phys.* **123**, 084318 (2005).
- ⁴⁶S. N. Altunata, S. L. Coy, and R. W. Field, *J. Chem. Phys.* **123**, 084319 (2005).
- ⁴⁷C. H. Greene, *Phys. Rev. A* **28**, 2209 (1983). "The common thread in all R-matrix methods is their solution of the Schrödinger equation within a finite volume of configuration space. The scattering properties of a many particle system are known once the normal logarithmic derivative is specified on the surface enclosing the reaction volume." Eq. (19) of this reference defines the R-matrix in terms of wavefunction log-derivatives and eigenchannels.
- ⁴⁸A. J. Stone, *The Theory of Intermolecular Forces* (Oxford University Press, New York, 1997).
- ⁴⁹S. L. Coy, B. M. Wong, J. J. Kay, V. S. Petrović, and R. W. Field, (unpublished).
- ⁵⁰S. L. Coy, B. M. Wong, and R. W. Field, "A new one-electron effective potential for CaF based on ab-initio calculations," in *63rd OSU International Symposium on Molecular Spectroscopy* (Columbus, OH, USA 2009), http://molspect.chemistry.ohio-state.edu/symposium_64/symposium/Program/MI.html#MI07.
- ⁵¹Additional details regarding the differences and conversion between these two quantum defect formulations can be found in the more extensive Appendix A of Ref. 38.
- ⁵²J. K. G. Watson, *Mol. Phys.* **81**, 277 (1994).
- ⁵³E. V. Akindinova, V. E. Chernov, I. Yu. Kretinin, and B. A. Zon, *Phys. Rev. A* **81**, 042517 (2010).
- ⁵⁴B. A. Zon, *Zh. Eksp. Teor. Fiz.* **102**, 36 (1992); Sov. Phys. JETP **75**, 19 (1992).
- ⁵⁵B. A. Zon, *Phys. Lett. A* **203**, 373 (1995).
- ⁵⁶J. Dubau, *J. Phys. B* **11**, 4095–4107 (1978).
- ⁵⁷W. Kohn, *Phys. Rev.* **74**, 1763 (1948).
- ⁵⁸R. Guérout, Ch. Jungen, H. Oueslati, S. C. Ross, and M. Telmini, *Phys. Rev. A* **79** 042717 (2009).
- ⁵⁹C. H. Golub and C. F. Van Loan, *Matrix Computations*, p. 582, Johns Hopkins University Press, Baltimore, Second Edition, 1989.